Karlsruhe Institute of Technology
Faculty Mechanical Engineering, Institute for Neutron Physics and Reactor Technology

Instituto Tecnológico de Buenos Aires
Escuela de Postgrado, Maestría en Energía y Ambiente

Master Thesis

Thermohydraulic Investigation on the use of Carbon Dioxide as Coolant for a solid Breeding Blanket for DEMO

Autor: Felix Caspari
felix.caspari@online.de

Supervisors: Dr. Lorenzo V. Boccaccini, KIT
Dr. Francisco A. Hernandez Gonzalez, KIT
Prof. Cecilia Smoglie, ITBA

Submission date: 31.08.2017

Preface and Acknowledgements

This thesis is part of my Master in Mechanical Engineering at the Karlsruhe Institut for Technology (KIT). The thesis was written at the Campus Nord of KIT at the Institute for Neutron Physics and Reactor Technology.
I would like to thank my supervisors, Prof. Robert Stieglitz and Dr. Lorenzo Boccaccini. Prof. Stieglitz made this thesis possible by awakening my interest in the topic of nuclear fusion during his lectures. Dr. Boccaccini was thankfully willing to accept my application for a Master Thesis over Skype, since I was doing a semester abroad during my search for a thesis. I would also like to thank Francisco Hernandez Gonzalez for answering my many questions and always having an open ear for my problems. Last but not least, Florian Schwab and my other colleagues at INR welcomed me with open arms and made my time there very enjoyable.

I Abstract

The Helium Cooled Pebble Bed (HCPB) Breeding Blanket (BB) is one of the 4 BB concepts being investigated in the EU for their possible implementation in a demonstration nuclear fusion reactor (DEMO).
The choice of He as fluid coolant for the BB is motivated by a virtually complete transparency to neutrons, leaving unaffected the T production capabilities of the blanket, as well as chemical inertness, molecular stability under high temperatures and neutron irradiation and a superior heat conductivity and capacity, leading to the best cooling performance in terms of heat transfer capabilities among other gas cooling choices. However, this cooling performance figure is hindered by the very low density of the gas, which leads to large pressure drops and high pumping power, thus affecting the overall plant efficiency, as well as to chronic leakages and large coolant inventories. These disadvantages, together with the still immature technology readiness of the respective turbomachinery, the price of this coolant, as well as its recognized limited resources pose concerns about the use of He as coolant for a BB in DEMO.
On the other side, carbon dioxide has been the fluid coolant choice since the 50's in the nuclear fission industry for gas cooled reactors (MAGNOX, AGR). Despite its lower heat capacity and thermal conductivity (about 22% and 17% of that of helium respectively), its larger density (11 times larger molecular weight for CO_2) can lead to an advantageous performance on heat dissipation rate per unit of pumping power. This feature, coupled with its relative transparency to neutrons, the molecular stability at the operating temperatures of the BB and the industrial scale ready turbomachinery makes CO_2 an attractive alternative to He. The feasibility of a CO_2-cooled breeding blanket is assessed in this work from the point of view of the thermohydraulic performance.

II Table of contents

III List of Figures

1 Introduction

With global warming and ocean acidification due to man-made CO_2 being one of the most pressing concerns of our time, increased focus has been put on research into energy sources that emit little to no CO_2. One of the options for energy production being evaluated is nuclear fusion. The organisation ITER, comprised of China, the EU, India, Japan South Korea, Russia and the USA, has the goal of building a working fusion reactor. As a first step, the International Thermonuclear Experimental Reactor (ITER) will be built in southern France. While this reactor will not be used to produce net electrical energy for the grid, it should allow major steps forward in our understanding of plasma physics and the design of technical components. The next step after experimenting with ITER is building a Demonstration Power Plant (DEMO), which is envisioned to demonstrate the viability of commercial fusion plants by feeding up to 1.5 GW of electrical energy into the grid and showcasing a "closed fuel cycle", which means that it will breed the tritium that is required for the fusion reaction during its operation.

One of the most important parts of a fusion reactor is its hull containing the plasma. The inside of this hull is lined with so called breeding blankets (BBs). The two main function of these blankets is breeding the tritium needed for the fusion reaction and dissipating the huge heat flows caused by said reaction. The tritium breeding is done by having a lithium core capture a neutron emitted in the fusion reaction. The lithium core then decays into an alpha particle and a tritium core. Cooling channels traversing the blanket dissipate the heat introduced by both the fusion reaction and the tritium breeding. The main structural material of the BB is Eurofer97, a specialized low-activation steel that is designed to withstand neutron fluxes over extended periods of time. The Karlsruhe Institute of Technology (KIT) has developed a blanket concept for ITER that uses a lithium ceramic as the breeding material and is cooled by helium, the Helium-Cooled-Pebble Bed Test Blanket Module (HCPB TBM).

Helium offers some key advantages as a cooling medium. It is virtually completely transparent to neutrons, which facilitates the tritium breeding in the blanket. Furthermore, it is stable even at high temperatures and the neutron fluxes typically present in fusion reactors, chemically inert and posesses high heat conductivity and capacity. A difficulty in using helium is its very low density, which leads to chronic leakages, a large coolant inventory and difficulty to achieve high heat transfer rates without incurring high pressure drops. This means the overall plant efficiency suffers due to the high necessary circulating power. Another factor is the limited helium supply and its high price. Due to these disadvantages, carbon dioxide has been considered as an alternative coolant medium. Although it has a lower heat capacity and thermal conductivity, it has the potential to offer a higher heat dissipation rate per unit of pumping power due to its higher density. Thanks to be-

ing the coolant of choice for advanced nuclear fission concepts, there is readily available industrial scale turbomachinery for CO_2. Combined with its acceptable transparency to neutrons and molecular stability in the operating temperature of the BB (≈300-500°C) range makes CO_2 an interesting alternative to helium as a cooling medium.
The focus of this thesis will be the thermohydraulic study of a unit slice of a HCPB TBM using CO_2 as coolant. The unit slice was used for CFD analysis with helium before, so a comparison of the results will be done. A global temperature increase is expected due to the worse heat transfer capabilities of CO_2. In a second step, ways to increase the heat transfer capabilities of the channel walls will be proposed and the thermohydraulic performance of the optimized blanket with CO_2 cooling will be assessed by means of available correlations.

1.1 Nuclear Fusion

Nuclear fusion is in many ways the opposite of nuclear fission, which is already widely used to produce energy. Instead of splitting one heavy nucleus into two lighter ones, two light nuclei are combined into one heavy one. Fusion reactions can be endo- or exothermic, but for the purpose of energy generation only exothermic fusion reactions are interesting. Those fusion reactions are also the energy source of the sun and other stars.
How likely the occurrence of a fusion reaction between two nuclei is is determined by their reaction cross section, which is highly energy dependend. Because of that, most fusion reactions can only take place at extremely high pressure and temperature, since the nuclei have to overcome the coulomb barrier. The coulomb barrier is the energy barrier due to electrostatic interaction that the two nuclei need to overcome so they can get close enough to undergo a nuclear reaction, as illustrated in Figure 1.

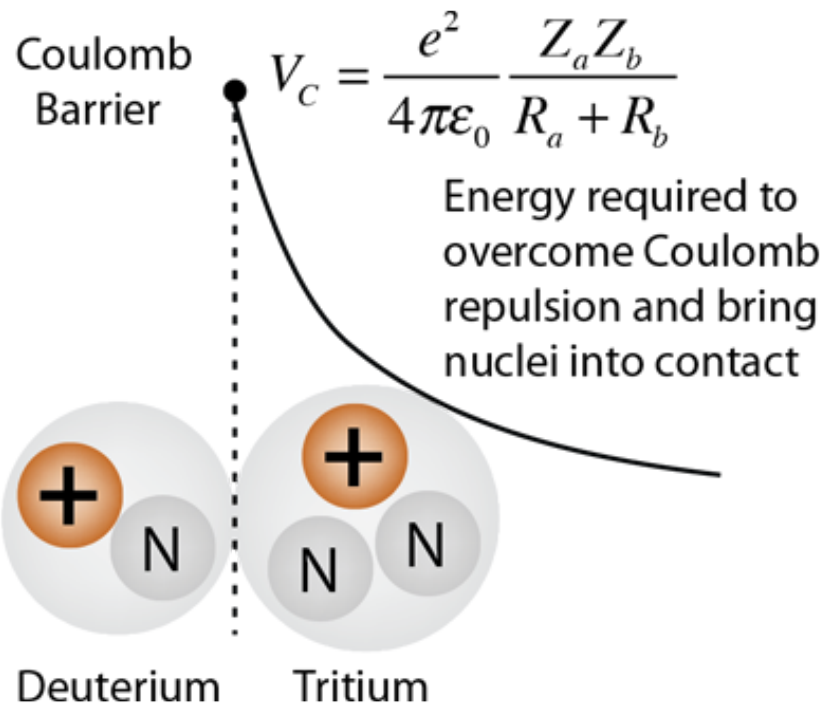

Figure 1: Illustration of the coulomb barrier for a D-T reaction [1]

The key requirement for an exothermal fusion reaction is that the binding energy per nucleon is lower for the pre-fusion nuclei than for the after-fusion nucleus. This means that the nuclei that fuse together have to be lighter than ^{56}Fe, since that nucleus has the highest binding energy per nucleon as shown in Figure 2. Similarly, an exothermic fission reaction can only occur with a nucleus heavier than ^{56}Fe.

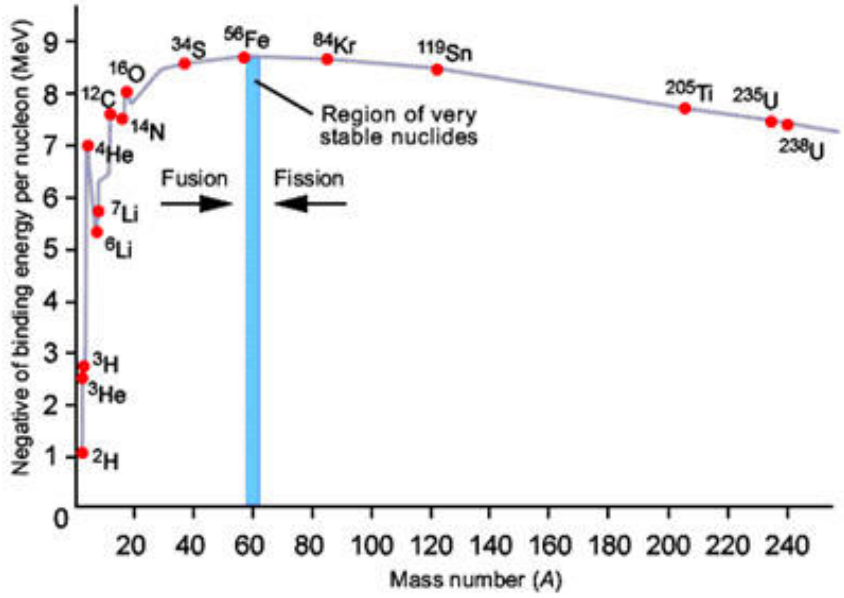

Figure 2: Average binding energy per nucleon as a function of atomic mass [2]

The reason why the binding energy per nucleon has a maximum at ^{56}Fe is because there is a conflict between the strong nuclear force and the electromagnetic force between the protons in the nucleus. Since the strong nuclear force only has a very limited reach, it only affects directly adjacent nucleons. The electromagnetic force on the other hand has a very long reach, meaning that larger nuclei become less stable due to it wanting to separate the nucleons from each other.
As can be seen from Figure 2, ^{4}He shows a local maximum in binding energy per nucleon. Furthermore, hydrogen and its isotopes have only one proton per atom, meaning that it has the lowest electromagnetic repulsion. This makes a fusion reaction of two hydrogen isotopes with ^{4}He as a result particularly interesting for energy production. Due to the particularly high cross section of deuterium ($^2_1$H or $^2_1$D) and tritium ($^3_1$H or $^3_1$T) those two isotopes are the preferred fuel for a hydrogen-to-helium fusion reaction. Figure 3 illustrates the cross sections of different fusion reactions.
Deuterium is a stable naturally occurring isotope of hydrogen with an additional neutron. About 0.0156% of the naturally occurring hydrogen is deuterium, which means that it can feasibly be extracted from water in meaningful quantities. Tritium on the other hand is a radioactive isotope with a half life of 12.32 years. Due to this short half life it needs to be produced through a nuclear reaction to sustain the fuel needs of a fusion reactor.
The D-T fusion reaction fulfils the following reaction equation:

$$^2_1D +^3_1 T \rightarrow^4_2 He + n + 17.6MeV \tag{1}$$

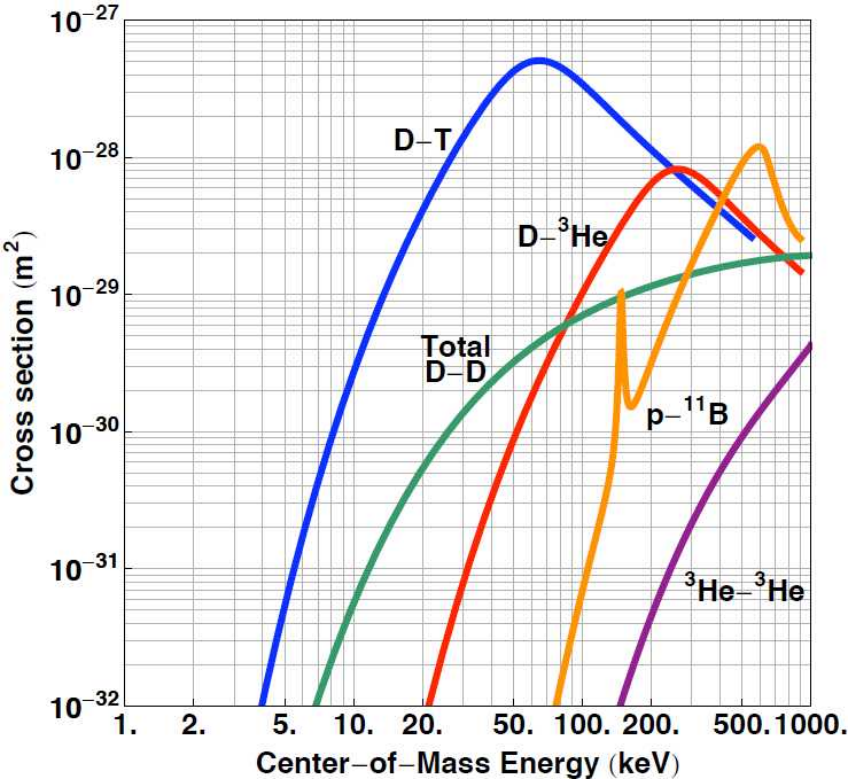

Figure 3: Cross section for a fusion reaction of different nuclei [3]

To allow a fusion reaction of the two nuclei, the D-T mix needs to be heated to very high temperatures while maintaing a good plasma density and confinement time so the coulomb barrier can be overcome. This means that the fuel mix will be in a plasma state. The energy necessary to overcome the maximum of the coulomb barrier between a deuterium and a tritium nucleus is 415keV. This would mean that the plasma would have to have a temperature of around 4.6 billion Kelvin, which would make fusion on earth extremely challenging. In reality, fusion reactions already occur at energies around 10-20 keV due to the tunnel effect, so a plasma temperature of roughly 115-230 million Kelvin is enough. This is still a very high temperature, but it can be achieved by enclosing the plasma in an electromagnetic field to minimize conductive heat losses. The plasma can be heated by different methods, for example ohmic heating, microwaves or neutral beam injection.

1.2 Plasma Confinement

The two main plasma confinement methods used to research fusion reactions are either intertial confinement or electromagnetic confinement. This thesis will focus on electromagnetic confinement.

There are varying concepts for the shape of the electromagnetic field containing the

plasma. Early fusion experiments often used a magnetic mirror setup, where magnets are set up in such a way that the density of the magnetic field lines increases towards the ends of the confinement area, as shown in Figure 4. This will cause the particles in the plasma to experience an increasing force preventing them from leaving the containment the closer they get to its edge. However, only particles within a certain energy range and angle of approach to the end of the confinement will be successfully reflected. Particles outside this range can leave the plasma, meaning that this configuration will always have some losses at the ends. This lead to an increased focus on circular plasma shapes where such end losses are nonexistent.
A short overview over the two main concepts for circular plasma confinement will be given in the following subsections.

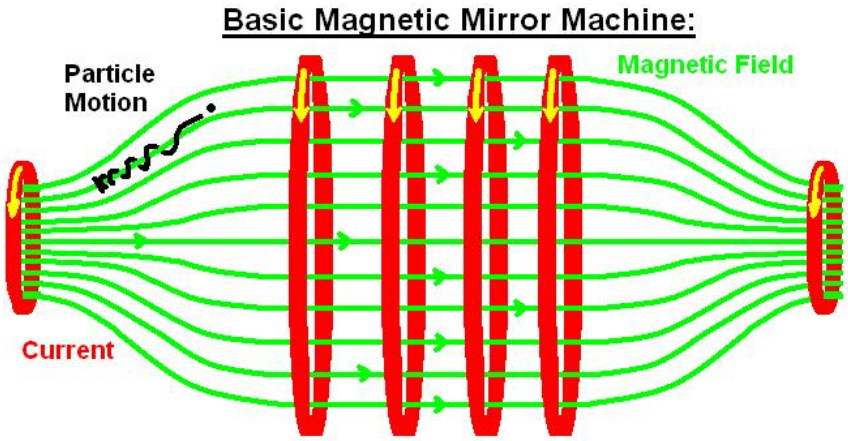

Figure 4: Magnetic mirror setup with exemplary particle track [4]

1.2.1 Stellarator

The main problem with a circular or annular plasma confinement is that the density of the magnetic field lines will decrease towards the outside of the confinement area, leading to a particle drift to the outside of the plasma. To counteract this drift, a Stellarator uses a complicated magnetic field to twist the plasma around itself, forcing particles to move from the outside to the inside of the plasma ring.

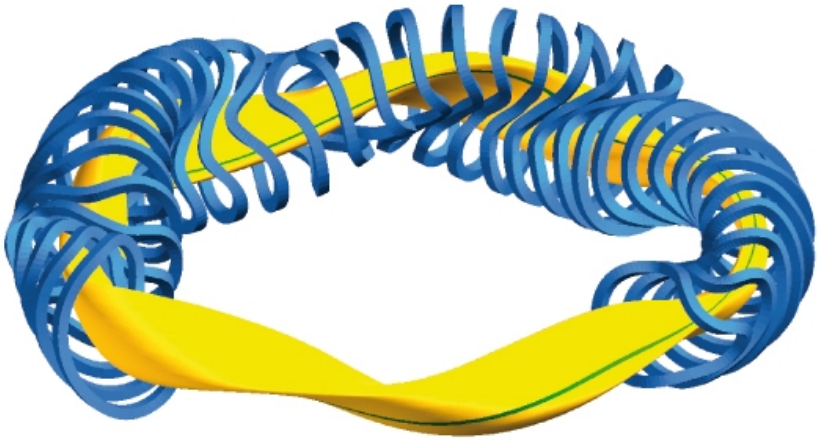

Figure 5: Stellarator setup with exemplary magnetic field line in green [5]

After initial successes, the Stellarator configuration showed problems with far higher plasma losses than theoretically predicted. Together with its very complex plasma physics and engineering, this lead to a reduced interest in the Stellarator setup for a few decades, especially due to the Tokamak showing far more promising results. Since the 1990s research into the Stellarator has increased again because new methods of construction (especially increased computing power allowing better simulations) have led to an improved quality of the magnetic fields, facilitating a better plasma confinement. The most modern current research reactor that uses a Stellarator configuration is Wendelstein 7-X, located in Greifswald, Germany.

1.2.2 Tokamak

The Tokamak concept of magnetic confinement was developed in the USSR in the 1950s. Their name comes from the Russian abbreviation of "toroidal chamber with magnetic coils". When Soviet scientists presented their results at the 1968 IAEA International Conference on Plasma Physics and Controlled Nuclear Fusion Research, showing an electron temperature in excess of 1000eV, western scientists were first skeptical because they were not even close to achieving that in their Stellarator setups. However, after an analysis with laser scattering measurements by British scientists invited to the USSR confirmed the results, most research into Stellarators was abandoned and the Tokamak became the dominant confinement concept.

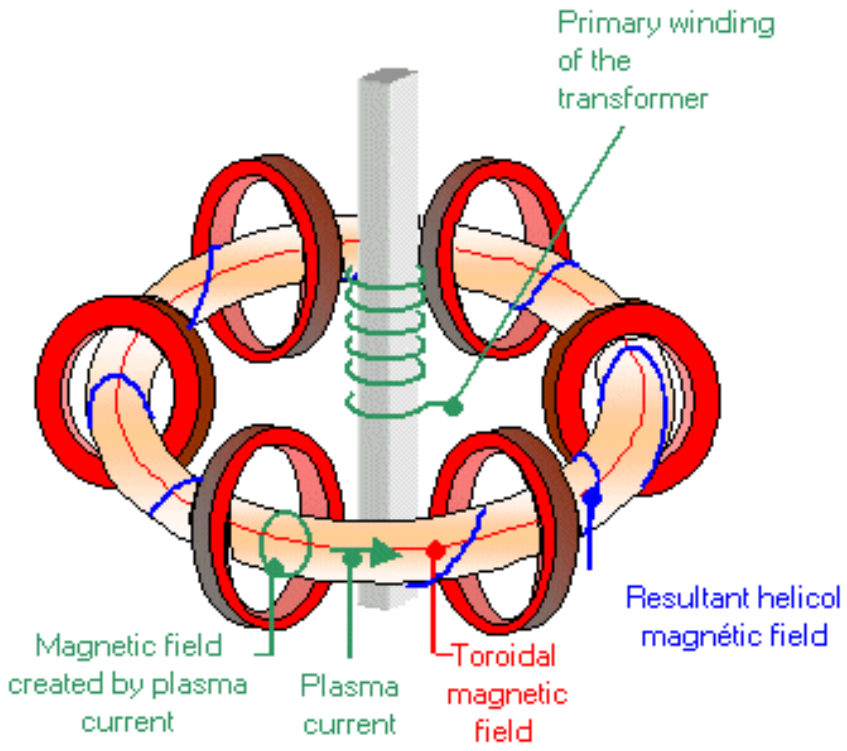

Figure 6: Tokamak setup with exemplary magnetic field line in blue [6]

Instead of using a twisted outer magnetic field to compensate the particle drift in the plasma like the Stellarator, the Tokamak employs a current running through the plasma to twist the magnetic field lines around the plasma torus. This allows for considerably less complex magnet shapes, but also means that a tokamak operates in a pulsed manner while a stellarator can operate continuously. The biggest currently operating tokamak is the Joint European Torus (JET) in Culham, UK. ITER, which is supposed to show net energy gain through fusion (scientific break-even), is being built in Cardarache, France and is scheduled to be operational in 2025.

1.3 Tokamak Reactor Architecture

The Tokamak reactor studied in this thesis is DEMO. In the following paragraph a short overview over its reactor architecture will be given.

Figure 7 shows the overall reactor architecture. The fusion plasma is shown in a transparent purple color. Moving outwards, the breeding blankets are blue while the divertor at the bottom is pink. The main purpose of the breeding blankets is the production of tritium and the dissipation of heat produced by the fusion reaction while the divertor extracts heat and ash produced by the fusion reaction and minimizes the plasma contamination. The green layer directly outside of the blankets and divertor is the vacuum vessel, with its access ports shown above and below the main structure. The purple and

brown components are the electromagnets responsible for generating the electromagnetic field used to contain the plasma. The reactor housing is shown in dark grey.

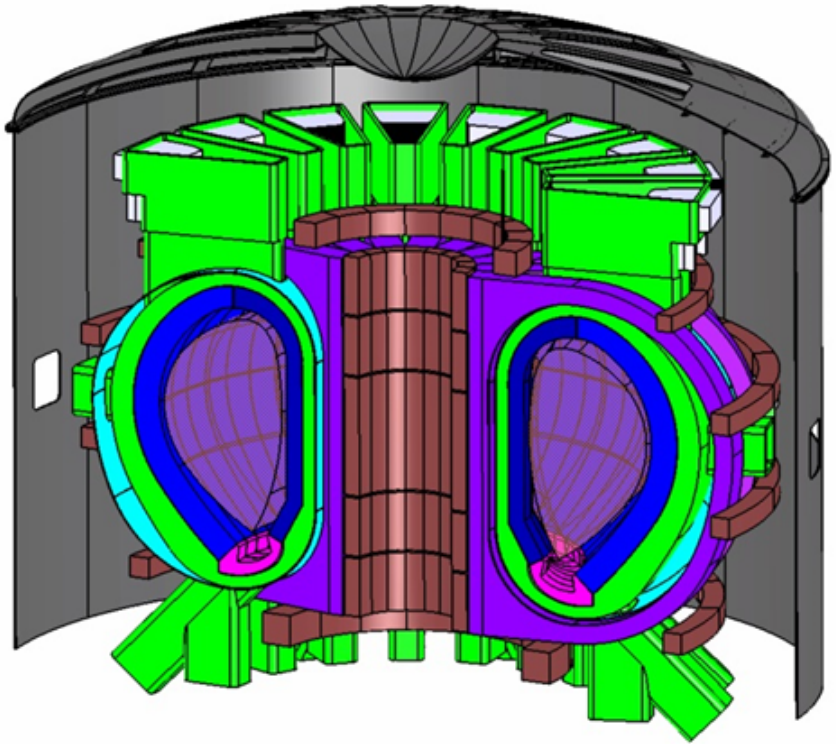

Figure 7: An overview of the DEMO reactor architecture

1.4 Tritium Breeding

Due to the low half-life of tritium (12.32 years), it does not naturally occur in sufficient quantities to fulfil the fuel requirements of a nuclear fusion reactor for energy production. This means that the reactor needs to produce enough tritium to ensure self-sufficiency. The reaction used to produce tritium in a fusion relies on using litium and the neutron produced in the fusion reaction (see Equation (1)). Tritium can be produced from both naturally occurring litium isotopes according to the reaction equations

$$^{6}Li + n \rightarrow T + \alpha + 4.78MeV \tag{2}$$

$$^{7}Li + n \rightarrow T + \alpha + n - 2.47MeV \tag{3}$$

However, the breeding reaction using ^{7}Li is endothermal while the breeding reaction with ^{6}Li is exothermal. Furthermore, the breeding reaction ^{6}Li has a much higher cross-section, shown in Figure 8, which is important to achieve a good tritium breeding ratio.

$$\text{TBR} = \frac{\text{Number of tririum atoms produced}}{\text{Number of fusion reactions}} \tag{4}$$

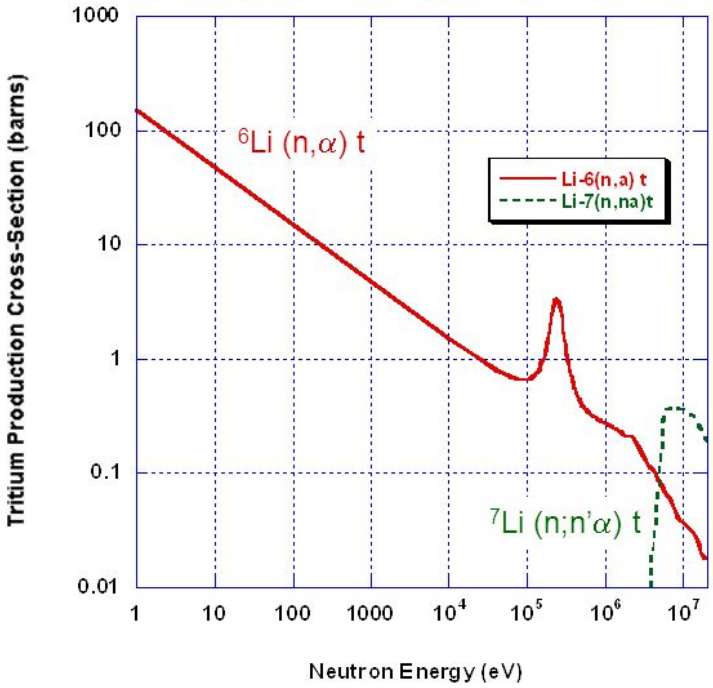

Figure 8: Cross-sections for the tritium breeding reaction using lithium

Due to these factors, the lithium used in tritium breeding for DEMO will be enriched to a ^{6}Li content of 60% to ensure good thermal efficiency and a TBR greater than 1.1.

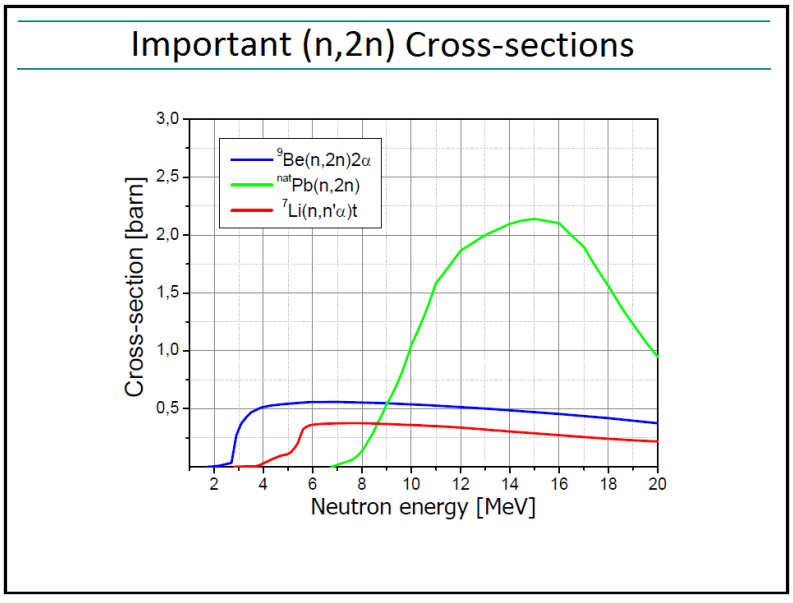

Figure 9: Cross-sections for a (n,2n) reaction in lead and beryllium [7]

To achieve a sufficient number of breeding reactions, the very high-energy neutrons emitted from the fusion plasma need to be moderated to allow for a high reaction cross section

and multiplied to reach a sufficient number of neutrons. The two main materials used as neutron moderators and multipliers are beryllium and lead. Figure 9 shows the neutron multiplication cross-section for the two materials. Lead has the advantage of having a very high cross-section for neutron multiplication, but this is only true and higher neutron energies. Unfortunately, this means that neutrons that have been moderated by collisions with other nuclei before reaching the neutron multiplication material will not be able to triccer such a reaction in lead. Beryllium, however, will allow such moderated neutrons to trigger a neutron multiplication reaction but does not have such a high peak cross-section.

1.5 Breeding Blankets

1.5.1 Functions

The so called breeding blankets (BBs) are modules covering most of the plasma-facing wall of the fusion reactor vessel. They have three main functions:

1. Producing enough tritium with the neutrons produced in the fusion reaction to ensure the reaction self-sufficiency
2. Produce high-grade heat and transfer it for use in a power generation cycle.
3. Shielding the parts immediately behind the BB from radiation while also contributing to the shielding of the supercoducting magnet coils.

1.5.2 Types of Breeding Blankets

There are different designs for the BBs. The ones being developed in Europe both use helium as a coolant while differing in their choice of breeding material, other designs use water as their coolant. Focusing on the BB designs being developed in Europe, one design uses a lead-lithium mix liquid metal as the breeding/neutron multiplication material while the other one uses lithium orthosilicate pebbles as the breeding material and beryllium pebbles for neutron multiplication. This thesis will focus on the helium cooled pebble-bed breeding blanket (HCPB BB).

1.5.3 Helium Cooled Pebble-Bed Breeding Blanket

The breeding blankets cover almost all the interior of the vacuum vessel as shown in Figure 10. They are divided into interior and exterior segments, consisting of seven and eight blanket modules respectively. There are 20mm gaps between the segments to allow for remote handling operations.

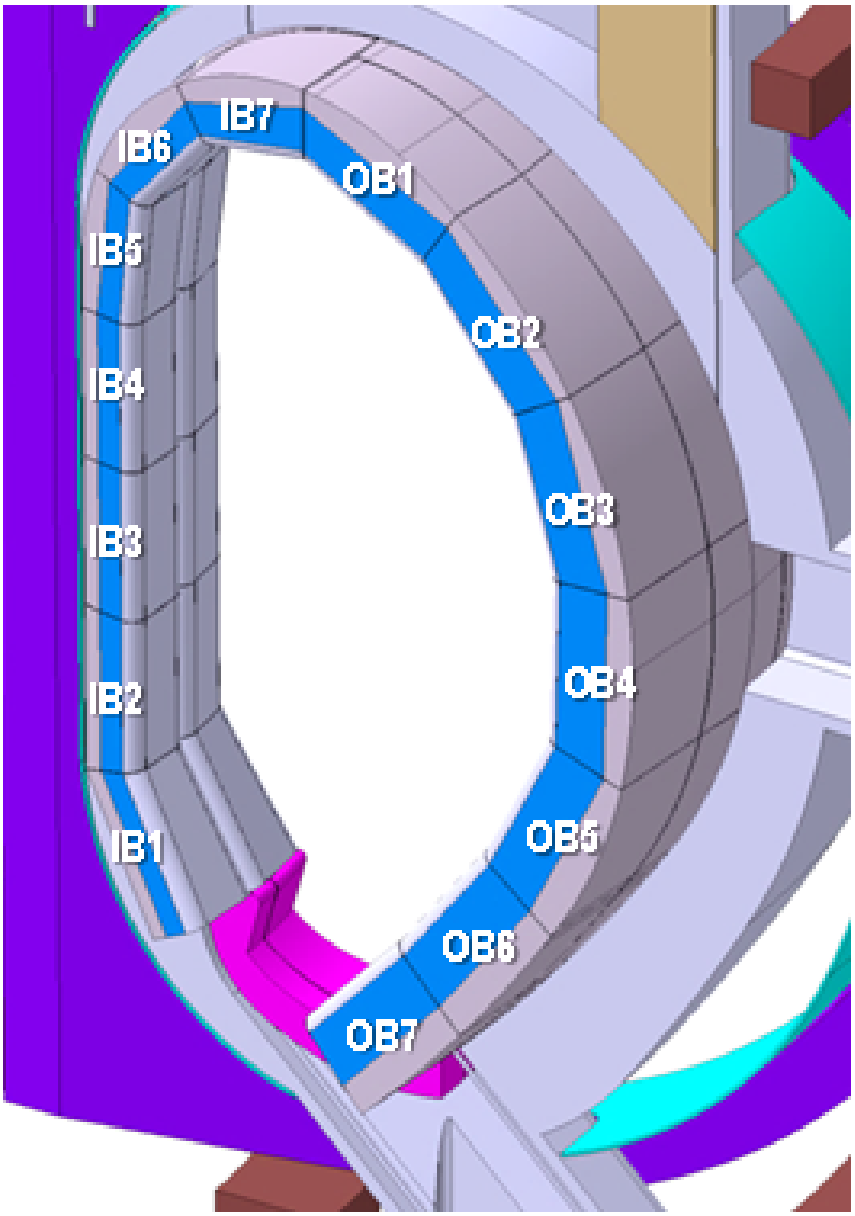

Figure 10: Blanket layout in DEMO

Looking closer at one of the BB modules (in this case OB4), one can see the layered setup of the module. Behind the first wall (the part of the module closest to the plasma) and its tungsten armor, there are alternating beryllium and lithium orthosilicate pebble beds with cooling plates between them. Figure 11 shows the overall layout and the layering in the BB module.

Since the layout of the BB module is symmetrical, the thermohydraulic analysis done in this thesis can be done on a representative slice of the BB module shown in Figure 12. It consists of half of a lithium orthosilicate pebble bed, one cooling plate, half of a beryllium pebble bed and the corresponding parts of the first wall and the back supporting structure.

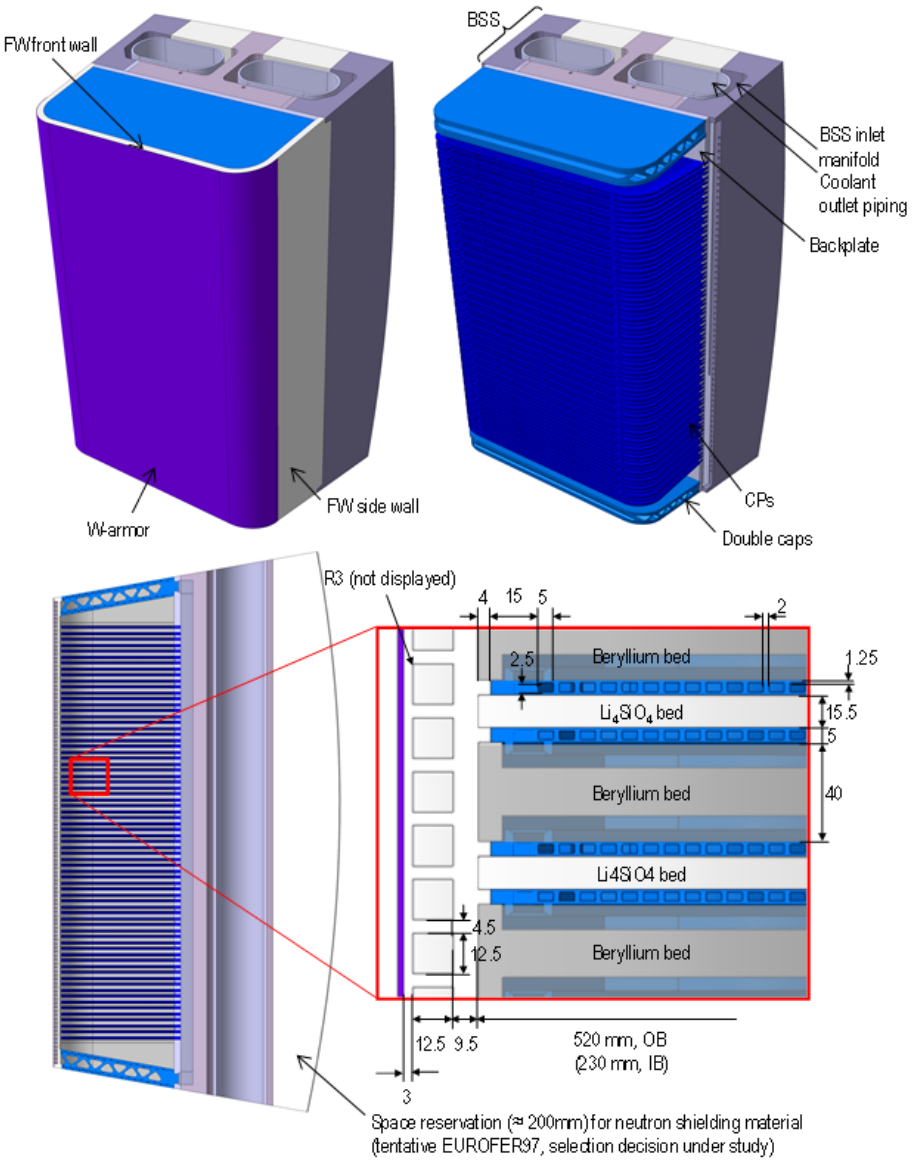

Figure 11: BB module layout and layering

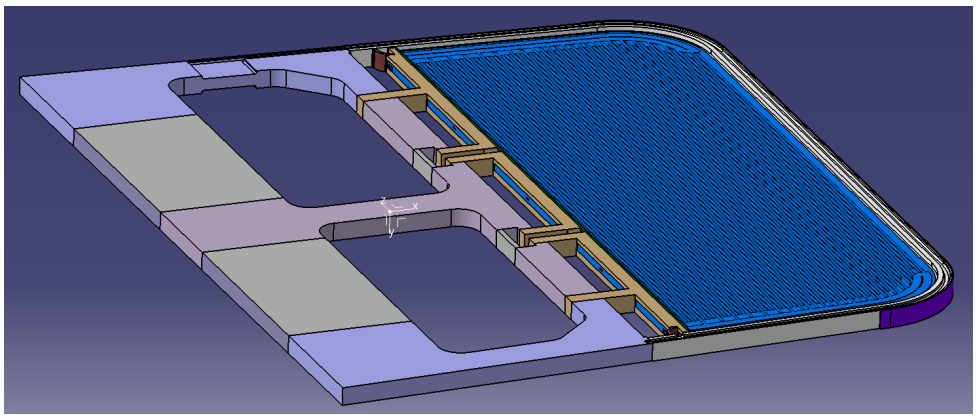

Figure 12: Representative slice of the HCPB BB

Temperature design limits have been determined for the materials in the BB to ensure the chemical and mechanical stability of the blanket. For Eurofer97, the specialized steel that the first wall, cooling plate and most of the back supporting structure are made of, an operating temperature range of 300-550°C is given. This allows the steel to resist damage from the high neutron fluxes while keeping enough mechanical strength to withstand the forces affecting the blanket. For the pebble beds of beryllium and lithium orthosilicate, the limiting factors are the stability of the material and the mechanical stresses introduced by thermal expansion of the pebbles. This leads to design limit temperatures of 650°C for beryllium and 920°C for lithium orthosilicate. To ensure that the Eurofer97 does not cool below 300°C, the inlet temperature of the coolant is set to that temperature. For the outlet temperature a value greater than 500°C is desired to provide high quality heat for power generation.

2 Theory

2.1 Governing Equations for Fluid Dynamics

2.1.1 Conservation Equations for Mass, Momentum and Energy

The three conservation equations for mass (5), momentum (6) and energy (7) are the basis for describing fluid flows [8]. They are obtained by considering the fluid as a continuum and applying the conservation of mass, momentum and energy.

$$\frac{\partial \rho}{\partial t} + \frac{\partial \rho u_i}{\partial x_i} = 0 \tag{5}$$

$$\frac{\partial \rho u_i}{\partial t} + \frac{\partial \rho u_j u_i}{\partial x_j} = -\frac{\partial p}{\partial x_i} + \frac{\partial \tau_{ij}}{\partial x_j} + \rho S_i \tag{6}$$

$$\frac{\partial \rho h}{\partial t} + \frac{\partial \rho u_i h}{\partial x_i} = \frac{\partial p}{\partial t} + \frac{\partial \tau_{ij} u_i}{\partial x_j} - \frac{\partial \dot{q}_i}{\partial x_i} + \rho u_i S_i \tag{7}$$

ρ is the density of the fluid, t is the time, x_i (i = 1,2,3) are the cartesian coordinates, u_i is the velocity in the direction of the cartesian coordinates, p is the static pressure, τ_{ij} is the stress tensor, S_i is the source term for the body forces in the direction of x_i and $\dot{q}_i$ is the heat flow in the direction of i. τ_{ij} depends on the shear rate in Newtonian fluids:

$$\tau_{ij} = \left[\mu\left(\frac{\partial u_i}{\partial x_j} + \frac{\partial u_j}{\partial x_i}\right)\right] - \frac{2}{3}\mu\frac{\partial u_k}{\partial x_k}\delta_{ij} \tag{8}$$

μ is the dynamic molecular viscosity and δ_{ij} is the Kronecker delta, which takes the value $\delta_{ij} = 1$ for $i = j$ and $\delta_{ij} = 0$ for all other cases.

Newtonian fluids have linear and inelastic flow properties. Their shear rate is proportional to the shear stress. They can be characterized by their viscosity, which mainly determines their inner friction and depends on the temperature T and the pressure p, although the sensitivity to pressure only appears at very high pressures.

In a perfect gas the specific enthalpy is given by:

$$dh = c_p dT \tag{9}$$

The heat flow $\dot{q}_i$ is given by Fourier's law of heat conduction:

$$\dot{q}_i = -\lambda\frac{\partial T}{\partial x_i} \tag{10}$$

Since the Mach numbers of the fluid flows are significantly lower than 0.3, the flow can be treated as incompressible [8]. This means that equations (5), (6) and (7) can be simplified

to the following:

$$\frac{\partial u_i}{\partial x_i} = 0 \tag{11}$$

$$\rho \frac{\partial u_i}{\partial t} + \rho u_j \frac{\partial u_i}{\partial x_j} = -\frac{\partial p}{\partial x_i} + \frac{\partial}{\partial x_j}\left[\mu\left(\frac{\partial u_i}{\partial x_j} + \frac{\partial u_j}{\partial x_i}\right)\right] + \rho S_i \tag{12}$$

$$\rho c_p \frac{\partial T}{\partial t} + \rho c_p u_i \frac{\partial T}{\partial x_i} = u_i \frac{\partial}{\partial x_j}\left[\mu\left(\frac{\partial u_i}{\partial x_j} + \frac{\partial u_j}{\partial x_i}\right)\right] + \frac{\partial}{\partial x_i}\left(\lambda \frac{\partial T}{\partial x_i}\right) + \rho u_i S_i \tag{13}$$

Given that the density in an incompressible flow is constant, its time derivative disappears. Now the pressure is not linked to density and temperature by a constituive equation, meaning that the energy conservation equation (13) is independent of the other equations. This means that an incompressible flow without an addition of heat can be calculated with just the conservation equations for mass (11) and momentum (12). Using all three equations (11), (12) and (13), all incompressible, transient three-dimensional flows involving friction can be calculated if the boundary conditions and initial values are known. This applies to laminar, transitional and turbulent flows. The solution to the Navier-Stokes equations is an open problem and can currently only be approached numerically.

2.1.2 Turbulent Flow

A turbulent flow is a three-dimensional flow of fluids involving turbulence. Its main characteristics are:

1. They are three-dimensional and in a stochastically nonsteady state. While the average of the flow field over time can be constant, the momentary flow field varies significantly in all three dimensions.
2. Much more kinetic flow energy is lost in a turbulent flow compared to a laminar flow due to the shear movement of the fluid increasing the friction losses. Kinetic energy is transformed into internal energy of the fluid, raising its temperature.
3. Turbulent flows are well suited for mixing processes and to increase the heat transfer of surfaces, since the turbulence mixes the fluid several orders of magnitude better than molecular diffusion processes do.

To achieve turbulent flow, a certain minimum flow speed must be met. The Reynolds number Re is used to determine whether that speed has been reached. It is a dimentionless number describing the ratio of the force of inertia to the viscous or friction force. For a

turbulent flow in a channel, Re is defined as

$$Re = \frac{\rho u d_h}{\mu} \tag{14}$$

ρ is the fluid density, u is the fluid velocity, μ is the dynamic viscosity and d_h is the hydralic diameter of the channel, defined as

$$d_h = \frac{4A}{U} \tag{15}$$

with A being the channel area and U being its circumference.
The critical Reynolds number in the range of $Re_{crit} = 2000 - 3000$ is where a fully formed channeled flow goes from laminar to turbulent.
There are three main methods to calculate turbulent flows in CFD: Direct Numerical Simulation (DNS), Large Eddy Simulation (LES) and Reynolds Averaged Navier Stokes (RANS). Figure 13 shows the differences in precision when calculating a temperature at one point in a flow.

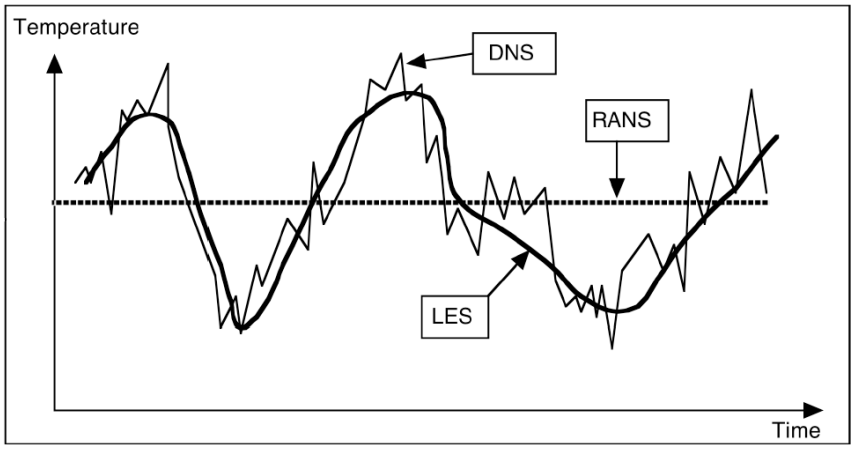

Figure 13: Differences between DNS, LES and RANS solutions [9]

A compromise needs to be found between precision and resources needed for the simulation. In most commercial CFD applications, the RANS method is used to simulate fluid flows. Since this thesis also uses that method, the turbulence models used in RANS will be explored in some more detail.

2.2 CFD Methods

2.2.1 Direct Numerical Simulation

This method is the most precise simulation, but also takes the longest times and needs very high computing power. It uses no turbulence models, meaning that even very small turbulences are fully solved, covering all time and lenght scales relevant in the problem.

To be able to calculate these very fine fluid movements, a DNS needs a fine mesh with very short time intervals. A measure for the lengths that the mesh needs to be able to map is the Komogorov length scale given by:

$$\eta = \left(\frac{\nu^3}{\epsilon}\right)^{0.25} \tag{16}$$

ϵ is the average of the dissipation rate per mass unit and ν is the kinematic viscosity.
The mesh does not necessarily have to be fine enough to resolve exactly that length scale, but its resolution has to be in the same order of magnitude as the Kolgomorov length scale [10]. This means that especially for high-Re problems a DNS needs an extremely high mesh size to allow for exact calculations
Errors in the simulation can occur due to incertainties in the boundary conditions and initial values or the numerical discretization or the analyzed volume. These errors are manageable since they can be estimated. The solution of the simulation is equivalent to a short term laboratory experiment.
Due to the very high costs associated with a DNS, it is mainly used when the other methods do not give precise enough results. This means its main use field is in research, ranging - among other things - from the laminar-turbulent transition over mechanisms of turbulence generation to the interdependency of combustion and turbulence.

2.2.2 Large Eddy Simulation

The LES is a middle ground between the very precise, but expensive and time-consuming DNS and the less precise, but fast RANS. The goal of a LES is calculating larger vortex structures that are more important for transport processes by directly resolving the larger length and time scales while describing the small vortoces through approximations and models. This is achieved by putting the fluctuations of the conserved quantities of a flow field through a low pass filter with regards to their size.
The LES is mainly applied in situations where a DNS cannot be done due to a very complex geometry or high Reynolds numbers, but higher precision is needed than a RANS can deliver. While it still necessitates a three-dimensional time dependend calculation of the flow field, it is far less resource intensive than a DNS.

2.2.3 Reynolds Averaged Navier Stokes

The turbulence is modeled by averaging the transient Navier-Stokes equations over time, giving the Reynolds Averaged Navier-Stokes equations. This is achieved by dividing the momentary values of the flow field into an average value and a stochastic fluctuation value. This leads to all the linearly fluctating values being eliminated from the resulting set of

partial differential equations. Since the convective terms in the Navier-Stokes equations are not linear they remain and have to be evaluated with special turbulence models.

2.3 Stochastic Turbulence Models used in RANS

Since a RANS simulation is used in this thesis, the turbulence models used in that method will be described in further detail.
Osbourne Reynolds, after whom the Reynolds number is named, considered turbulence to be the result of stochastic fluctuations in a fluid flow. This means that all variables in a flow can be expressed the sum of a time-independent average value and an associated fluctuation value:

$$\Phi(x_i, t) = \bar{\Phi}(x_i) + \Phi'(x_i, t) \tag{17}$$

In stochastically steady-state flows the average value can be expressed as:

$$\bar{\Phi}(x_i) = \lim_{T\to\infty} \frac{1}{T} \int_0^T \Phi(x_i, t)dt \tag{18}$$

T is the averaging interval. T needs to be big enough that the calculated average value is independent of the starting point of the averaging.
For stochastically transient flows this method of averaging over time cannot be used. What is needed is a so called ensemble average:

$$\bar{\Phi}(x_i) = \lim_{N\to\infty} \frac{1}{N} \sum_{n=1}^{N} \Phi_n(x_i, t) \tag{19}$$

This is similar to repeating an experiment under the same conditions and averaging the results. N needs to be big enough to eliminate fluctutations while still allowing for a good resolution of the flow values. Figure 14 illustrates the different methods used for steady-state and transient flows.

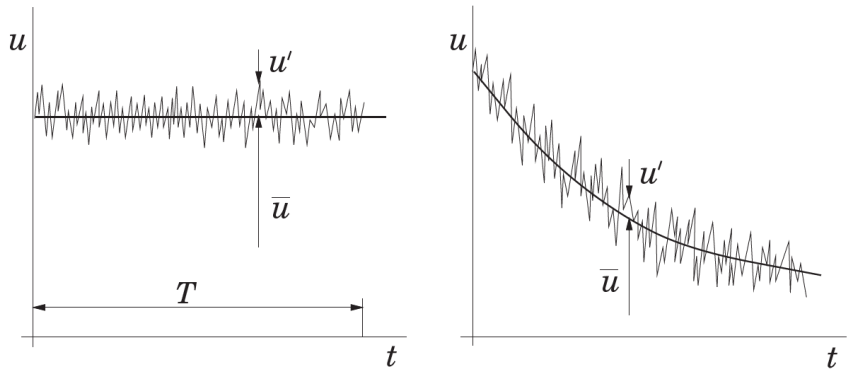

Figure 14: Time average of a steady-state (left) and ensemble average of a transient (right) flow value [8]

Using these averaging methods on the incompressible conservation equations gives:

$$\rho \frac{\partial \bar{u}_i}{\partial x_i} = 0 \tag{20}$$

$$\rho \frac{\partial \bar{u}_i}{\partial t} + \rho \bar{u}_i \frac{\partial \bar{u}_j}{\partial x_j} = -\frac{\partial p}{\partial x_i} + \frac{\partial}{\partial x_j}\left[\mu\left(\frac{\partial \bar{u}_i}{\partial x_j} + \frac{\partial \bar{u}_j}{\partial x_i}\right) - \rho\overline{u_i' u_j'}\right] + \rho S_i \tag{21}$$

$$\rho c_p \frac{\partial \bar{T}}{\partial t} + \rho c_p \bar{u}_i \frac{\partial \bar{T}}{\partial x_i} = \frac{\partial}{\partial x_i}\left(\lambda \frac{\partial \bar{T}}{\partial x_i} - \rho c_p \overline{u_i' T'}\right) + \bar{u}_i \frac{\partial}{\partial x_j}\left[\mu\left(\frac{\partial \bar{u}_i}{\partial x_j} + \frac{\partial \bar{u}_j}{\partial x_i}\right)\right] + \rho \bar{u}_i S_i \tag{22}$$

While these equations look fairly similar to the original ones, there are new unknown terms in both the momentum conservation equation (21) and the energy conservation equation (22). This means that there are more unknowns than equations, which makes the set of equations not self-contained anymore. The new unknowns are the Reynolds Stress Tensor (RST) and the turbulent heat flux density:

$$\tau_{turb} = -\rho\overline{u_i' u_j'} \tag{23}$$

$$q_{turb} = \rho c_p \overline{u' j T'} \tag{24}$$

The Reynolds Stress tensor is a momentum transfer term while the turbulent heat flux density describes the heat transfer through turbulence.
To solve the set of equations, one can deduce a conservation equation for the Reynolds Stress tensor from the Navier-Stokes equations, a so called Reynolds Stress Model, but this is highly complex. Another method is approximating the tensor through a turbulent viscosity model, which is used in the simulation in this thesis.

2.4 Turbulent Viscosity Models

The basic assumption of turbulent viscosity models is that the Reynolds Stress is caused by similar phenomenons as the shear stress. A second assumption is that the same

turbulence responsible for momentum transfer is also responsible for the transfer of heat. The transfer of mass, momentum and energy in laminar flows and their dissipation is mainly determined by the fluid's viscosity. Because of that, the effects of turbulence can be described by an increased viscosity. The Boussinesq approximation defines the RST as:

$$\tau_{turb} = -\rho\overline{u_i' u_j'} = \mu_t \left(\frac{\partial \bar{u}_i}{\partial x_j} + \frac{\partial \bar{u}_j}{\partial x_i} \right) - \frac{2}{3}\rho\delta_{ij}k \tag{25}$$

k it the turbulent kinetic energy defined as:

$$k = \frac{1}{2}\overline{u_i' u_j'} \tag{26}$$

μ_t is the turbulent dynamic viscosity that describes the increase in viscosity by turbulence. It is not a property of the fluid, like the dynamic or static viscosity, but varies with the flow conditions. There are different approaches to modeling the turbulent dynamic viscosity. Analogous to Fourier's law used in Equation (10), q_{turb} can be defined as:

$$q_{turb} = -\lambda_t \frac{\partial \bar{T}}{\partial x_i} \tag{27}$$

λ_t is the turbulent thermal conductivity given by:

$$\lambda_t = \frac{c_p \mu_t}{Pr_t} \tag{28}$$

The turbulent Prandtl number Pr_t is:

$$Pr_t = \frac{\overline{u_i' u_j'}}{\overline{u_j' T'}} \frac{\overline{\frac{\partial \bar{T}}{\partial x_j}}}{\overline{\frac{\partial \bar{u}_i}{\partial x_j}}} = \frac{\nu_t}{a_t} \tag{29}$$

a_t is the turbulent thermal diffusivity defined as:

$$a_t = \frac{\lambda_t}{\rho c_p} \tag{30}$$

The kinetic turbulent viscosity ν_t connected to the dynamic turbulent viscosity μ_t:

$$\nu_t = \frac{\mu_t}{\rho} = u_{turb} l_{turb} \tag{31}$$

u_{turb} and l_{turb} are the turbulent speed and a characteristic lenght for the turbulence. According to Diez [11], the turbulent Prandtl number Pr_t is assumed to be $Pr_t = 1$, so $\nu_t = a_t$ follows. This is a good approximation, since real-world values of the Prandtl

number tend to 1.
There are different approaches to obtaining the value of μ_t. They can be divided into Zero-, One- and Two-Equation Models, named after the number of partial differential equations that need to be solved in addition to the conservation equations.
An example for a Zero-Equation Model would be Prandtl's mixing-lenght concept. The advantage of such a model is its simplicity, which means it's very economical. They are rarely applicable in the real world though, because they need empirical input and do not consider the transport of turbulence, meaning that the turbulence has to be in a local equilibrium.
One-Equation models usually solve a partial differential equation for the turbulent kinematic energy k, which allows them to include effects caused by turbulence transport by obtaining a value for the turbulent time-scale. They still need empirical input for the mixing lenght. An example would be the Spalart-Allmaras model.
Like in One-Equation models, Two-Equation models solve a partial differential equation for k. Solving a second differential equation, for example for the characteristic frequency ω or the dissipation rate ε of the turbulence, makes it possible to find the characteristic tubulent lenght and time-scale.
Since this thesis uses a Two-Equation model, the relevant models will be discussed in the following subsections.

2.4.1 k-ε Model

The k-ε model solves two equations for the kinetic energy k and the turbulent dissipation ε. The coefficients in these equations are empirically derived and valid for fully turbulent flows. While it is widely used due to its robustness, easy implementation and lower computational requirements, it has limitations regarding complex flows involving high pressure gradients or strong streamline curvatures.
The k-ε model assumes that the dynamic turbulent viscosity is given by:

$$\mu_t = C_\mu \frac{k^2}{\varepsilon} \tag{32}$$

The differential transport equations for k and ε are:

$$\frac{\partial \rho k}{\partial t} + \frac{\partial}{\partial x_j}\left(\rho u_j k\right) = \frac{\partial}{\partial x_j}\left[\left(\mu + \frac{\mu_t}{\sigma_k}\right)\frac{\partial k}{\partial x_j}\right] + P_k - \rho\varepsilon + P_{kb} \tag{33}$$

$$\frac{\partial \rho \varepsilon}{\partial t} + \frac{\partial}{\partial x_j}\left(\rho u_j \varepsilon\right) = \frac{\partial}{\partial x_j}\left[\left(\mu + \frac{\mu_t}{\sigma_\varepsilon}\right)\frac{\partial \varepsilon}{\partial x_j}\right] + \frac{\varepsilon}{k}\left(C_{\varepsilon 1} P_k - C_{\varepsilon 2}\rho\varepsilon + C_{\varepsilon 1} P_{\varepsilon b}\right) \tag{34}$$

$C_{\varepsilon 1}$, $C_{\varepsilon 2}$, σ_k and σ_ε are constants defined in the simulation program used, which in case of this thesis is ANSYS CFX.
P_k represents the turbulence production due to viscous forces and is modeled as:

$$P_k = \mu_t \left(\frac{\partial u_i}{\partial x_j} + \frac{\partial u_j}{\partial x_i} \right) \frac{\partial u_j}{\partial x_j} - \frac{2}{3} \frac{\partial u_k}{\partial x_k} \left(\mu_t \frac{\partial u_k}{\partial x_k} + \rho k \right) \tag{35}$$

In incompressible flows, $\frac{\partial u_k}{\partial x_k}$ is small, so the right part of the equation does not contribute significantly to the value of P_k.
P_{kb} and $P_{\varepsilon b}$ include the influence of buoyancy forces into the model. Since in the simulation used in this thesis buoyancy effects weren't taken into account, a more detailed explanation of these factors can be done without.

2.4.2 k-ω Models

The k-ω model solves two equations for the kinetic energy k and the turbulent frequency ω. By automatically switching between a wall function and a low-Reynolds number formulation based on grid spacing, it allows for a more accurate near-wall treatment. Additionally, it offers good numerical stability due to not employing damping functions. A disadvantage is that the model usually predicts flow separation too early and needs very good mesh resolution near the wall.
The k-ω models assumes that the dynamic turbulent viscosity is given by:

$$\mu_t = \rho \frac{k}{\omega} \tag{36}$$

The two differential transport equations used are:

$$\frac{\partial \rho k}{\partial t} + \frac{\partial}{\partial x_j}(\rho u_j k) = \frac{\partial}{\partial x_j} \left[\left(\mu + \frac{\mu_t}{\sigma_k} \right) \frac{\partial k}{\partial x_j} \right] + P_k - \beta' \rho k \omega + P_{kb} \tag{37}$$

$$\frac{\partial \rho \omega}{\partial t} + \frac{\partial}{\partial x_j}(\rho u_j \omega) = \frac{\partial}{\partial x_j} \left[\left(\mu + \frac{\mu_t}{\sigma_\omega} \right) \frac{\partial \omega}{\partial x_j} \right] + \alpha \frac{\omega}{k} P_k - \beta \rho \omega^2 + P_{\omega b} \tag{38}$$

The model constants α, β, β', σ_k and σ_ω are defined in Ansys.

2.4.3 Shear Stress Transport (SST) Model

The SST model is based on the k-ω model and combines its advantages with the k-ε model by using a blending function. Near the wall the k-ω model is used, while farther away the k-ε model is used. This allows for a high accuracy in boundary layer simulations, but it still requires high mesh resolution near the wall.
Both the k-ε and the k-ω model overpredict the eddy viscosity because they do not account

for the transport of the turbulent shear stress. The SST model introduces a limiter to the formulation of the eddy viscosity:

$$\frac{\mu_t}{\rho} = \frac{a_1 k}{\max(a_1\omega, SF_2)} \tag{39}$$

a_1 and S are constants, while F_2 is the blending function used to combine the k-ε and k-ω model:

$$F_2 = \tanh\left(\left[\max\left(\frac{2\sqrt{k}}{\beta'\omega y}, \frac{500\nu}{y^2\omega}\right)\right]^2\right) \tag{40}$$

y is the distance to the wall.

The k-ε and k-ω models are combined by reformulating the k-ε model into a k-ω model and then dividing it by $(1 - F_2)$. The k-ω model is multiplied by F_2. Adding the two models yields:

$$\frac{\partial \rho k}{\partial t} + \frac{\partial}{\partial x_j}(\rho u_j k) = \frac{\partial}{\partial x_j}\left[\left(\mu + \frac{\mu_t}{\sigma_{k3}}\right)\frac{\partial k}{\partial x_j}\right] + P_k - \beta'\rho k\omega + P_{kb} \tag{41}$$

$$\begin{aligned}\frac{\partial \rho \omega}{\partial t} + \frac{\partial}{\partial x_j}(\rho u_j \omega) =& \frac{\partial}{\partial x_j}\left[\left(\mu + \frac{\mu_t}{\sigma_{\omega 3}}\right)\frac{\partial \omega}{\partial x_j}\right] \\ &+ (1 - F_2)2\rho\frac{1}{\sigma_{\omega 2}\omega}\frac{\partial k}{\partial x_j}\frac{\partial \omega}{\partial x_j} + \alpha_3\frac{\omega}{k}P_k - \beta_3\rho\omega^2 + P_{\omega b}\end{aligned} \tag{42}$$

2.5 Wall Treatment

The area near a wall is of utmost importance in modelling turbulence since in many configurations it is the main source of turbulence [12]. It also has a big influence on the calculation of wall heat transfer and friction coefficients.

The flow near a wall is characterized by high velocity gradients, going from high Reynolds numbers in the free stream area to low Reynolds numbers near the wall. Directly at the wall itself the no-slip condition determines that the velocity of the fluid must be zero. The area between the wall and the layer where the fluid velocity is 99% of the free stream velocity is called the boundary layer, visualized in Figure 15.

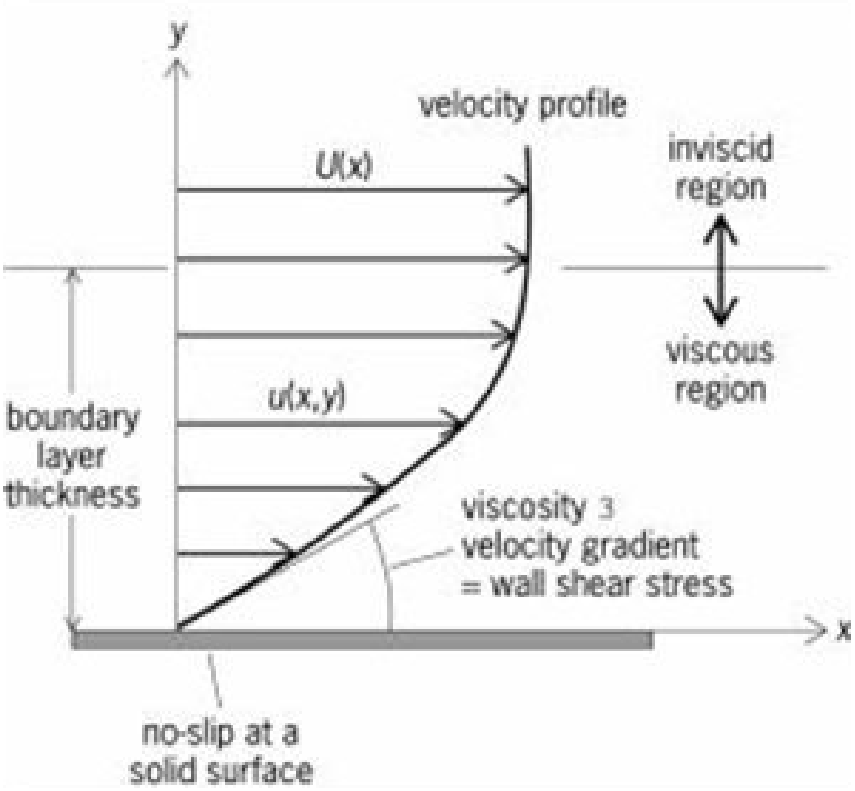

Figure 15: Velocity profile of a flow over a stationary surface [13]

In free flow conditions the friction caused by the viscosity of the fluid can usually be neglected since it is small compared to the friction caused by turbulence. Close to the wall turbulence is dampened, so the viscosity becomes important. This area is called the viscous region or viscous boundary layer. It exhibits a laminar flow where viscous friction dominates. The shear stress can be calculated by:

$$\tau = \mu \frac{\partial u}{\partial y} \tag{43}$$

Similar to this viscous boundary layer, a thermal boundary layer exists where there is a high temperature gradient. The relation between the viscous boundary layer and the thermal boundary layer is given by the Prandtl number Pr, as shown in Figure 16.

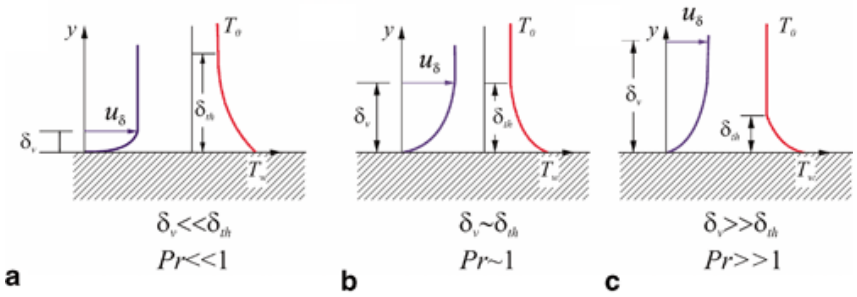

Figure 16: Illustration of viscous and thermal boundary layer for different Prandtl numbers [14]

The Prandtl number is defined as the proportion of kniematic viscosity ν and thermal diffusivity a:

$$Pr = \frac{\nu}{a} \tag{44}$$

ν represents the velocity field because it describes the friction caused by momentum transfer and that momentum transfer depends on the velocity field. Similarly, the thermal diffusivity represents the temperature field because it describes the heat transfer dependend on the temperature transfer, or rather dependend on the temperature difference. With

$$\nu = \frac{\mu}{\rho} \tag{45}$$

and

$$a = \frac{\lambda}{\rho c_p} \tag{46}$$

the Prandtl number can be expressed as

$$Pr = \frac{\mu c_p}{\lambda} \tag{47}$$

Since the Prandtl number of the carbon dioxide at 8.0MPa analyzed in this thesis is around $Pr = 0.74$, the behaviour of the gas lies somewhere between the cases (a) and (b) shown in Figure 16, though likely much closer to case (b).

The SST model uses is a two-layer model, which means that the size of the first cell of the mesh next to the wall should have a size of $y^+ \approx 1$. y^+ is the wall coordinate, the wall distance made dimensionless with the friction velocity u_τ and the kinematic viscosity ν.

$$y^+ = \frac{y u_\tau}{\nu} \tag{48}$$

$$u_\tau = \sqrt{\frac{\tau_w}{\rho}} \tag{49}$$

$$\tau_w = \mu \frac{\partial u}{\partial y} \tag{50}$$

Similarly, the velocity can be made dimensionless near the wall.

$$u^+ = \frac{u}{u_\tau} \tag{51}$$

Using these dimensionless values, a universal law of the wall has been found that gives a dimensionless near-wall velocity profile. This velocity profile is a very good approximation for natural streams in the region of the flow that is up to 20% of the total flow height. The profile, shown in Figure 17, can be divided into three sections. In the viscous sublayer up to $y^+ = 5$, $u^+ = y^+$ is valid. After a transition zone between $y^+ = 5$ and $y^+ = 30$, a logarithmic equation describes the relation between u^+ and y^+.

$$u^+ = \frac{1}{\kappa} \ln y^+ + B \tag{52}$$

κ is the von Kármán constant with a value of $\kappa = 0.41$. B is a constant dependend on the surface roughness. For smooth surfaces its value is $B \approx 5.5$.
The velocity in the transitional zone can be described by more complex equations, but this is beyond the scope of this thesis.

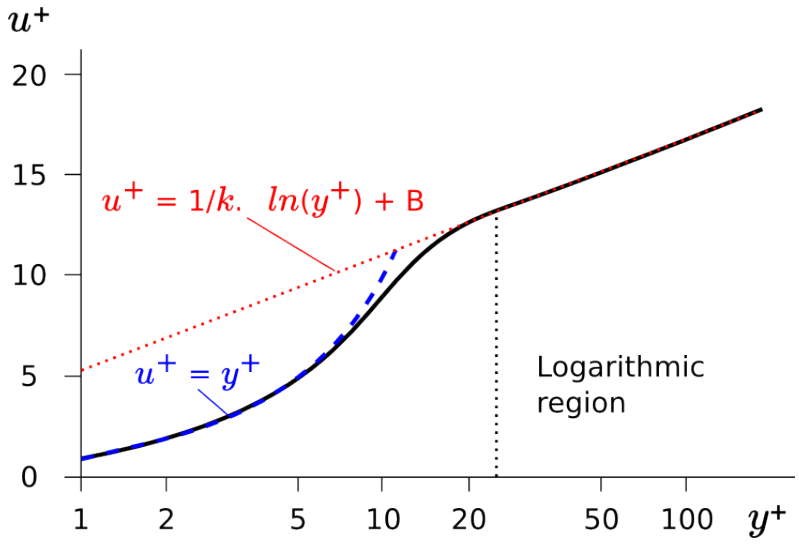

Figure 17: Dimensionless velocity profile of a flow near the wall [15]

2.6 Forced Convective Heat Transfer

Convective heat transfer, also called convection, is the transfer of heat through the movement of fluids. Heat can also be transfered by thermal conduction, but convective heat transfer is usually the dominant form of heat transfer in fluids. It is often described by

Newton's law of cooling, at least when the temperature changes are small, i.e. the heat transfer coefficient h is temperature independent.

$$\Delta Q = hA\Delta T \tag{53}$$

The heat transfer coefficient can be calculated in different ways. Often the Nusselt number is used. This dimensionless number expresses the ratio of overall heat transfer to conductive heat transfer.

$$Nu = \frac{hD_h}{k} \tag{54}$$

D_h is the hydraulic diameter of the channel while k is the thermal conductivity of the fluid. The hydraulic diameter of a rectangular channel can be calculated with

$$D_h = \frac{4A}{U} = \frac{2ab}{a+b} \tag{55}$$

with a and b being the side lenghts of the rectangle.
In laminar flows the Nusselt number is characteristically close to 1, meaning that most of the heat transfer occurs through thermal conduction. In turbulent flows it is typically in the range of 100-1000, showing that convective heat transfer dominates.
Forced convection differs from free convection in that the fluid transport motion in forced convection is generated by an external source, i.e. the fluid is pumped or sucked through a tube or over a surface. Different correlations have been found to calculate the Nusselt numbers for forced convective heat transfer in turbulent flows. Often the Gnielinski correlation is used, which offers very good approximations for Reynolds numbers up to 500000 and Prandtl numbers between 0.5 and 2000.

$$Nu = \frac{\frac{f}{8}(Re - 1000)Pr}{1 + 12.7\left(\frac{f}{8}\right)^{0.5}(Pr^{\frac{2}{3}} - 1)} \tag{56}$$

f is the Darcy friction factor. It can either be obtained from a Moody chart in channels with rough walls or through the Petukhov correlation for smooth channels.

$$f = (0.70\ln(Re) - 1.64)^{-2} \tag{57}$$

2.7 Effect of Roughness on Flow and Heat Transfer

As can be seen from the Gnielinski correlation, the Darcy friction factor f is an important factor in calculating the Nusselt number and thus the heat transfer. If the sand grain roughness ε of the channel walls and the Reynolds number are known, it can be obtained from the Moody diagram.

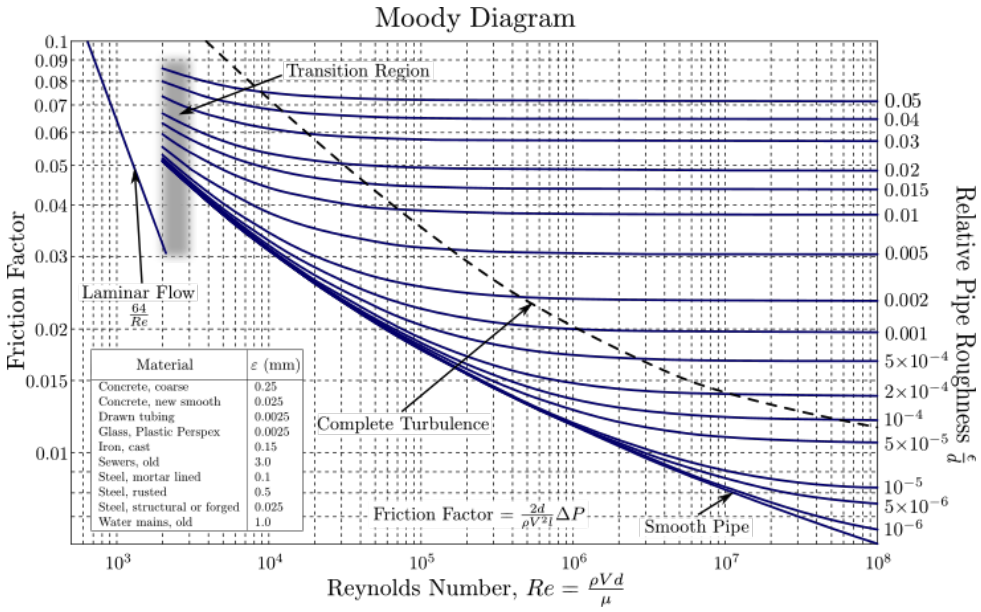

Figure 18: Moody diagram

The diagram is a graphical representation of the Colebrook-White equation, which provides a formula for the calculation of the Darcy friction factor that can be iteratively solved.

$$\frac{1}{\sqrt{f}} = -2\log\left(\frac{\varepsilon}{3.7D_h} + \frac{2.51}{Re\sqrt{f}}\right) \tag{58}$$

Fang et.al. [16] found a correlation allowing for a direct calculation of the Darcy friction factor.

$$f = 1.613\left[\ln\left(0.234\left(\frac{\varepsilon}{D_h}\right)^{1.1007} - \frac{60.525}{Re^{1.1105}} + \frac{56.291}{Re^{1.0712}}\right)\right]^{-2} \tag{59}$$

It is clear that a higher channel wall roughness will lead to a higher Darcy friction factor, which in turn will lead to a higher Nusselt number and thus higher heat transfer coefficient in the channel. This is explained by the fact that the main mechanism of heat transfer in the viscous sublayer of a turbulent flow is molecular diffusion, which is several orders of magnitude lower than the heat transfer achieved by forced convection. Increasing the roughness of the channel wall allows for breaking up of this viscous sublayer and trying to conduct hot fluid away from the wall while replacing it with colder fluid from the bulk of the flow. The increase in roughness can be done unstructured, but it is beneficial to use structures like ribs to introduce secondary flows mixing the fluid, as illustrated in Figure 19.

While the change in heat transfer can be assessed with the Nusselt number, the change in pressure drop is interesting to assess the overall thermal performance an artificial roughness offers. This change is correlated with the change in friction factor the artificial

roughness causes.

$$\Delta p = \frac{\dot{m}}{2\rho A}\frac{L}{D_h}f \tag{60}$$

To now assess the overall thermal performance of a roughened channel, i.e. comparing the increase in heat transfer with the incurred pressure loss penalty, the "thermal performance" metric TP is introduced.

$$TP = \frac{\frac{\overline{Nu}}{Nu_0}}{\left(\frac{\bar{f}}{f_0}\right)^{\frac{1}{3}}} \tag{61}$$

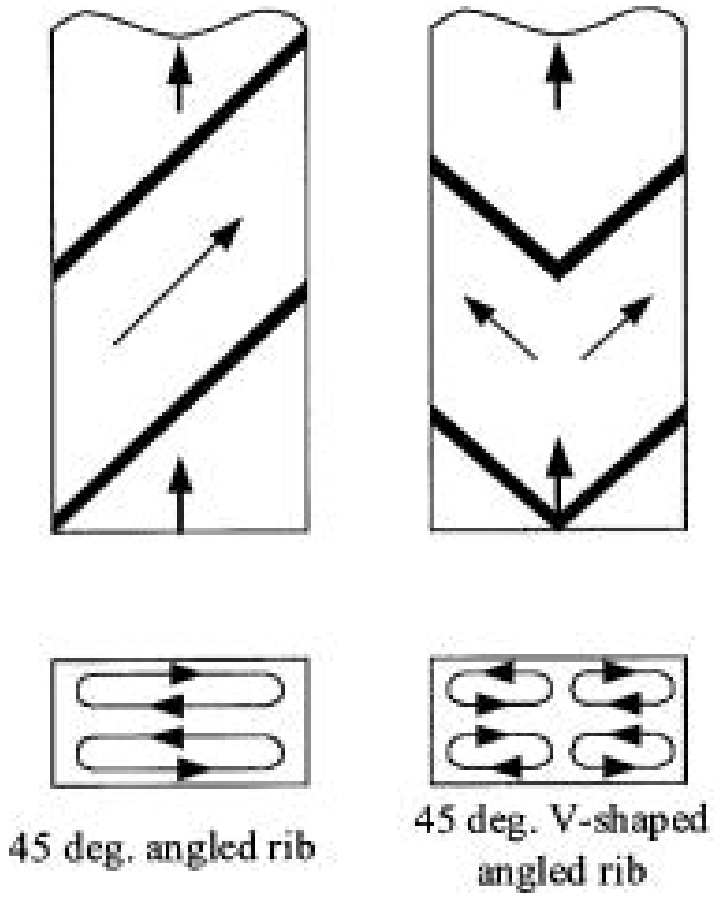

Figure 19: Secondary flows induced by ribs on the channel wall [17]

3 Numerical Simulation of a representative slice of a HCPB Breeding Blanket

3.1 Simulation Model

Since the main focus of this thesis is the comparison of the performance of helium cooling and CO_2 cooling, the same model of the HCPB BB as for the simulation of helium cooling at the Budapest University of Technology and Economics was used.

Due to the high accuracy needed in the simulation, a fine mesh is used. This would make a simulation of the whole BB extremely complex and time-consuming. Because of economic and temporal limitations a representative slice of the geometry is used, shown in Figure 20. It contains one cooling plate, half a layer of lithium orthosilicate and beryllium pebbles respectively and the corresponding parts of the back support structure and first wall.

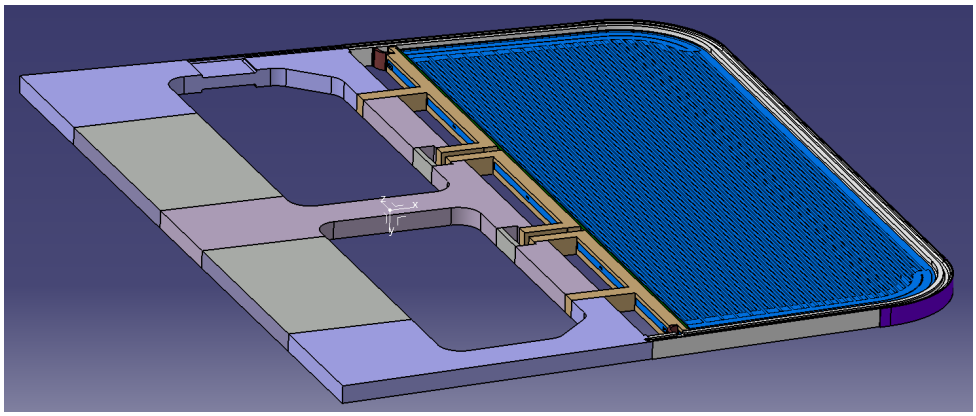

Figure 20: Representative slice of the HCPB BB

Inside the cooling plate are two counterflowing cooling loops. The coolant first passes through the first wall cooling channel and then through the cooling plate as shown in Figure 21.

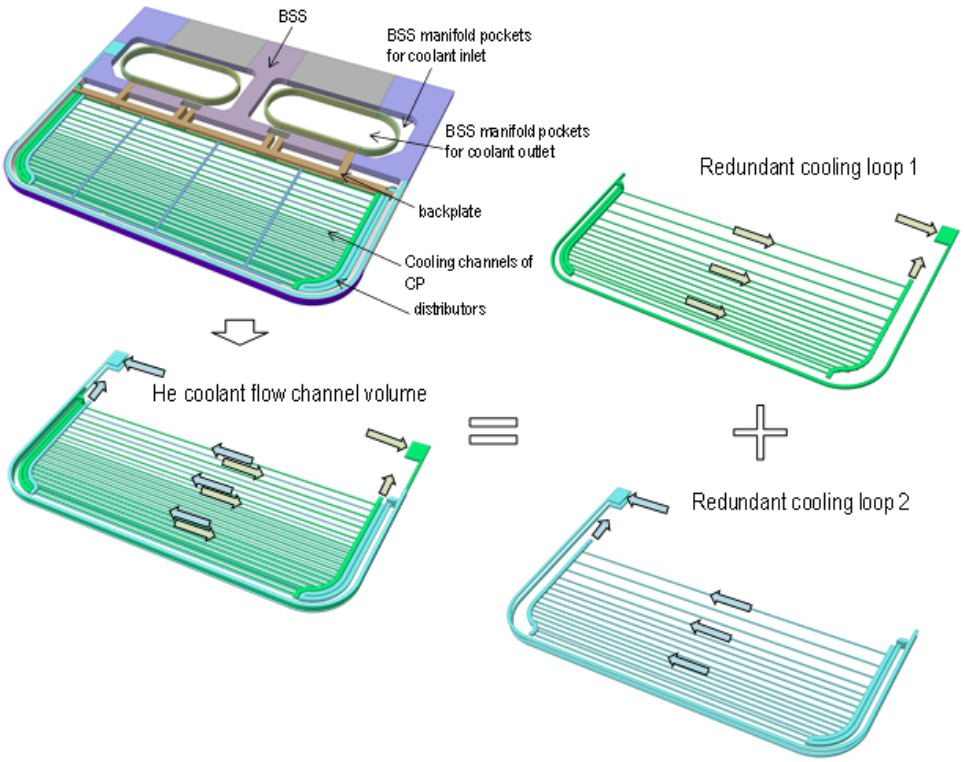

Figure 21: HCPB coolant flow scheme

3.1.1 Mesh

The mesh of this slice is a fully hexahedral mesh containing approximately 12.5 million nodes and 11.6 million cells. It has a minimum orthogonality angle of >20°, an expansion factor of <20 and a aspect ratio of <1000 in over 99% of its cells. Those values make it reasonable to expect an accurate and robust solution with very low discretization and round-off errors.

3.1.2 Physical Properties of Fluid and Solid

To determine the physical properties of carbon dioxide, the NIST Chemistry WebBook [18] was used. Firstly, the Mach number Ma is calculated to determine whether the flow can be treated as incompressible. This is the case if the Mach number is significantly lower than 0.3.

$$Ma = \frac{u}{a_s} \tag{62}$$

a_s is the speed of sound in the fluid. At 8.0MPa and 300°C (the entry temperature of the carbon dioxide), it is $a_s = 364.5\frac{m}{s}$. Combined with the flow velocity, this gives a Mach number of $Ma = 0.2$, so the flow can be treated as incompressible.
Since the simulation is set to treat CO_2 as a ideal gas, the density is calculated through

the ideal gas law using its molecular weight, which is set as $M(CO_2) = 44.01\frac{kg}{kmol}$.
The dynamic viscosity of CO_2 is taken from the NIST database, ranging from $\mu = 2.77 \cdot 10^{-5}$Pas at 300°C to $\mu = 3.93 \cdot 10^{-5}$Pas at 650°C. Since it depends on the temperature, its value is given in steps of 1K. Ansys CFX then interpolates the given values to determine the value it uses. Similarly, the thermal conductivity and the specific heat capacity are determined by interpolating values taken from the NIST database.
The structural material of the BB is Eurofer97, a specialized steel for nuclear applications. Its physical properties were retained from the previous simulation done at the Budapest University of Technology and Economics. While the specific heat capacity and thermal conductivity are again obtained by interpolation, the density is set as

$$\rho_{EF97} = 7751\frac{kg}{m^3} \tag{63}$$

The density of the lithium orthosilicate pebble bed was determined by using the density of lithium orthosilicate and the packaging density of the pebble bed. The obtained value was

$$\rho_{Li_4O_4Si} = 1526.4\frac{kg}{m^3} \tag{64}$$

The thermal conductivity was again determined by interpolating from a list of values. The same is true for the beryllium pebble bed. Since the thermal conductivity of beryllium pebble bed depends both on the temperature and the pebble bed strain, the beryllium zone is divided in three subzones. All the subzones have the same specific heat capacity and density, but the thermal conductivity is different. Both the thermal conductivity and specific heat capacity are obtained by interpolation from a list of values while the density is set to

$$\rho_{Be} = 1166.72\frac{kg}{m^3} \tag{65}$$

3.1.3 Boundary Conditions

3.1.3.1 Symmetries There are two main symmetry planes used in the simulation. They are located at the top and bottom of the HCPB BB slice. As the name symmetry plane implies, all values are mirrored. This is especially important in the fluid domains, since Ansys allows for no flows or scalar fluxes across such a symmetry plane, avoiding unwanted influeces of the limits of the simulation. If the symmetry boundary condition was not set, Ansys CFX would default to a no-slip boundary condition by default.

3.1.3.2 Thermal load The first wall of the blanket recieves a heat flux from the plasma radiation and charged particle collisions. On the straight part of the tungsten armor it is

set to

$$\phi_q = 500 \frac{kW}{m^2} \tag{66}$$

in agreement with the specifications for DEMO. On the curved part of the armor it is set in relation to the z-coordinate to account for the angle between heat flux and surface. The equation for the heat flux on the curved parts is

$$\phi_q = -2661748.2 \frac{W}{m^3} * z + 1907962.3 \frac{W}{m^2} \tag{67}$$

for the bend located in the negative z-coordinate and

$$\phi_q = 2661748.2 \frac{W}{m^3} * z + 1907962.3 \frac{W}{m^2} \tag{68}$$

for the bend located in the positive z-coordinate.
In addition to this heat flux from the plasma the slice is heated by neutrons being absorbed or moderated in the material and by nuclear reactions like the tritium breeding. This heating is modeled as a volumetric heating in the lithium orthosilicate, beryllium and Eurofer97. The amount of heat produced depends on the distance to the first wall, since the neutron flux gets lower farther away from the first wall. The values are obtained by interpolating data points and then added as a energy source to the lithium orthosilicate, beryllium and Eurofer97 subdomains.

3.1.3.3 Contact Interfaces

The contacts between the fluid and solid are modeled as non-slip walls with an equivalent sand roughness of 13.49 microns. The contacts between the solids are modeled as normal solid-solid contacts. Importantly, the thermal contact resistance between the pebble beds and the cooling plate is specified to account for the fact that it is not a solid beryllium or lithium orthosilicate material, but a pebble bed.

3.1.3.4 Inlet and Outlet Boundary Conditions

The inlet boundary condition for each coolant loop is set as a subsonic flow with a medium turbulence intensity of 5%. The temperature is 300°C and the mass flow is $\dot{m} = 0.1992 \frac{kg}{s}$. This mass flow was found by estimating the difference in specific heat capacity and thermal conductivity between helium and carbon dioxide and then multiplying the mass flow of helium with the obtained factor. The current settings lead to a outlet temperature of slightly over 500°C, so a further increase in mass flow is discouraged due to a requirement that the outlet temperature of the cooling fluid be over 500°C to allow for an efficient power cycle.
The outlet boundary condition is set to be subsonic and have a relative pressure difference

of 0 Pa when averaged over the whole outlet.

4 Results of the Simulation

4.1 Simulation with Initial Mass Flow Estimate

The results of the first simulation with a CO_2 mass flow of 0.1992 $\frac{kg}{s}$ showed the temperatures in the strucutural material exceed the design limit of 550°C. In the first wall, the maximum temperature was 585.29°C while the temperature of the cooling plate had a maximum of 592.74°C. The critical spots were at the front of the first wall, directly behind the tungsten armor and in the front third of the cooling plate, as shown in Figure 22. Ths slightly lower temperature of the first wall on the left side is explained by the flow direction of the cooling fluid in the cooling channel of the BB slice.

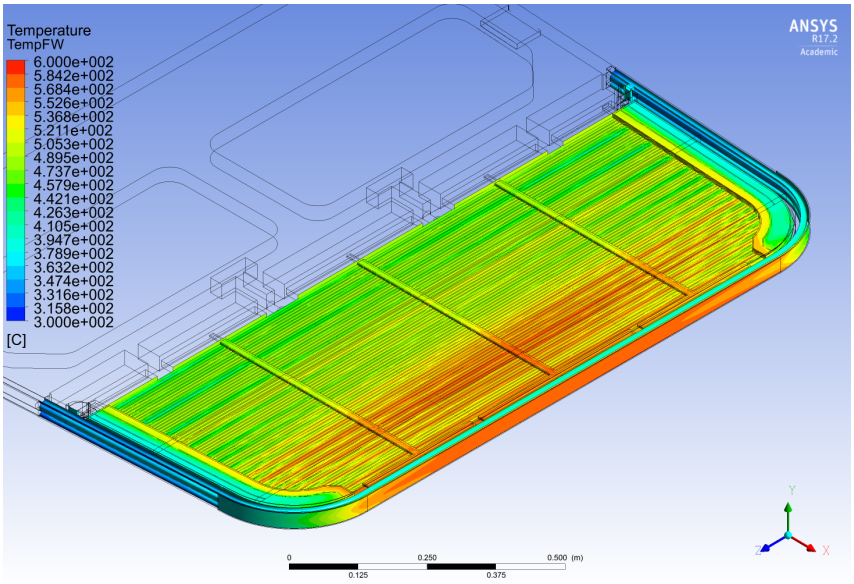

Figure 22: Temperature distribution in the cooling plate and the first wall

In the cooling plate, the temperature maximum was on the side contacting the lithium orthosilicate, which was to be expected since the tritium breeding reaction is exothermal and produces more heat than the moderation of neutrons in the beryllium. The temperature distribution reflects the layout of the cooling channels through the cooling plate.

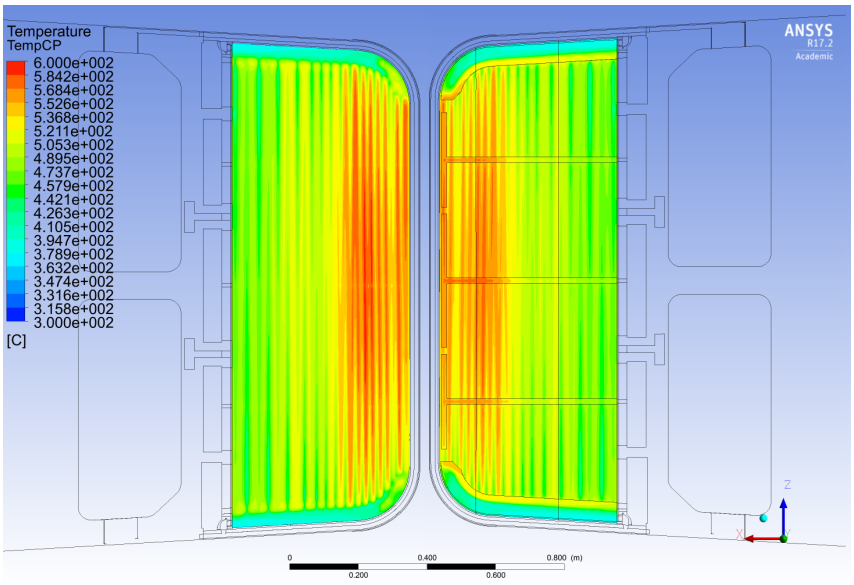

Figure 23: Temperature distribution of the cooling plate on the lithium orthosilicate (left) and beryllium (right) side

Both the lithium orthosilicate and the beryllium pebble bed also experience temperatures above the limits defined for them. The lithium orthosilicate reaches a temperature of 967.1°C while its allowed maximum temperature is 920°C. The beryllium is able to withstand temperatures up to 650°C, but gets up to 685.6°C. Again the critical region for the temperature is in the front third of the breeding/moderating zone.

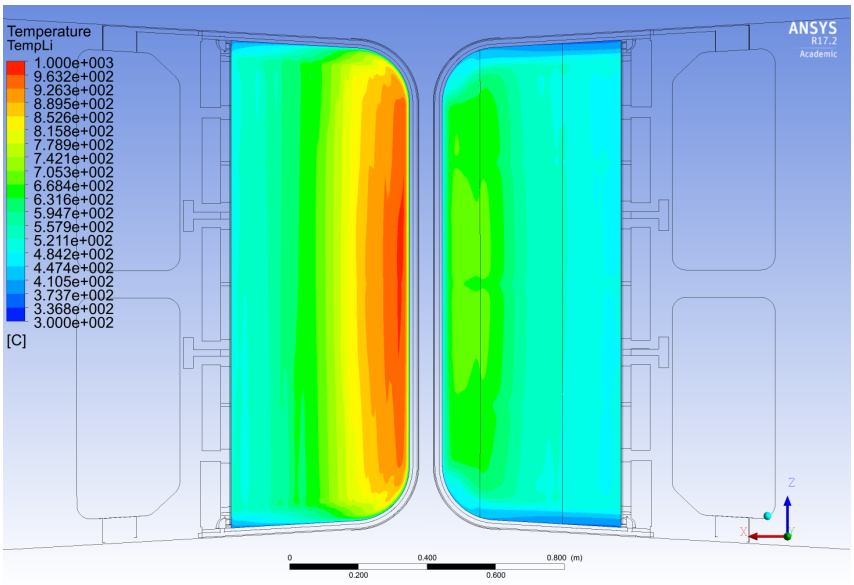

Figure 24: Temperature distribution of the pebble beds on the lithium orthosilicate (left) and beryllium (right) side

Finally, the temperature distribution of the CO_2 is shown in Figure 25. Since the fluid first passes through the first wall and then circulates through the cooling plate, the tem-

peratures reached in the first wall channels reach a maximum of 531.7°C adjacent to the wall, while its bulk temperature is 363.8°C. In the cooling plate, the CO_2 gets up to 583.3°C hot near the wall with the critical region again being in the front third of the BB. The bulk temperature is 533.1°C. However, since the fluid flows through cooler parts of the blanket on its way to the outlet, it leaves the blanket with a temperature of 506.6°C.

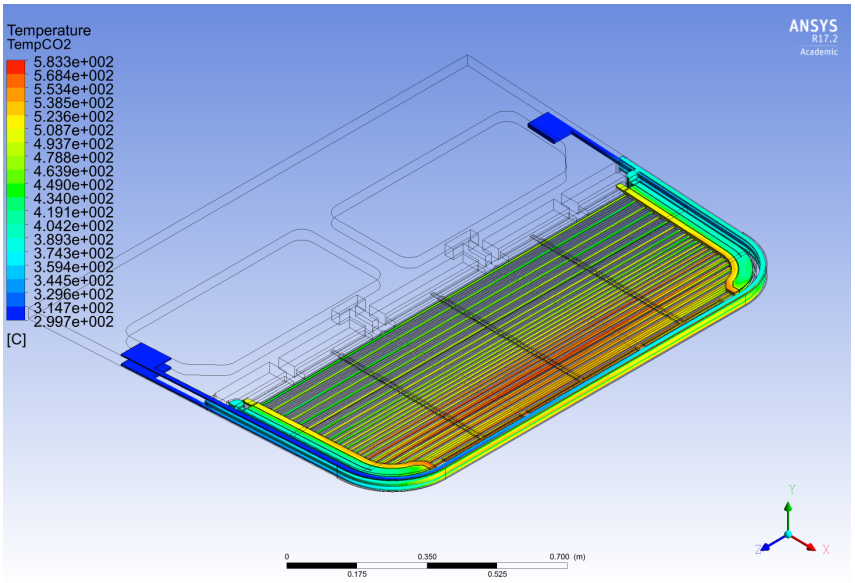

Figure 25: Temperature distribution of the CO_2

The current amount of heat transfer between fluid and solid is not enough to ensure a sufficient cooling of the critical spots of the blanket, located in the first wall and the front third of the breeding blanket. A possible way to increase the heat transfer would be to increase the mass flow. Examining the possibility of enhancing the heat transfer between solid and fluid by structuring the channel wall to break up the boundary layer will also be investigated.

The total pressure drop over the BB from inlet to outlet of the cooling loop is 0.266MPa.

4.2 Simulation with Increased Mass Flow

To lower the CO_2 bulk temperature and increase the heat transfer coefficient in the cooling channels, the mass flow of CO_2 was increased in an interative process until a mass flow was found that allowed for a sufficient cooling of the BB. The minimum mass flow leading to satisfactory results is $\dot{m}_{CO_2} = 0.23\frac{kg}{s}$. It offers Eurofer97, beryllium and lithium orthosilicate temperatures that are already very close to their respective design limits.
The temperature distribution in the cooling plate and the first wall is similar to the simulation with the original mass flow, but with lower temperatures overall. The maximum temperature reached in the first wall is 559.2°C while the cooling plate reaches a maxi-

mum of 557.7°C. Again the side of the cooling plate contacting the lithium orthosilicate reaches a slightly higher temperature than the side contacting the beryllium.

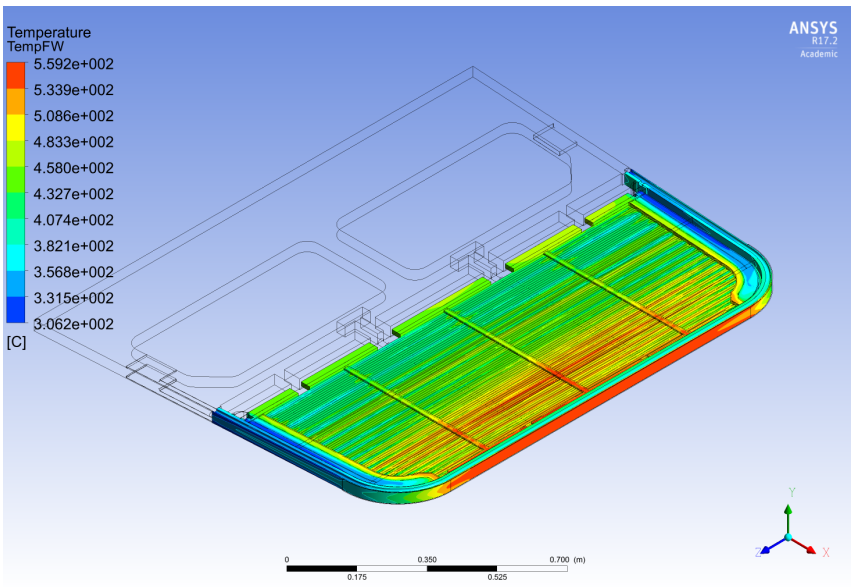

Figure 26: Temperature distribution of the cooling plate and first wall with $\dot{m}_{CO_2} = 0.23 \frac{kg}{s}$

Both the lithium orthosilicate and the beryllium pebble bed exceed their design limit temperatures of 920°C and 650°C respectively, reaching a maximum temperature of 945.9°C and 654.0°C.

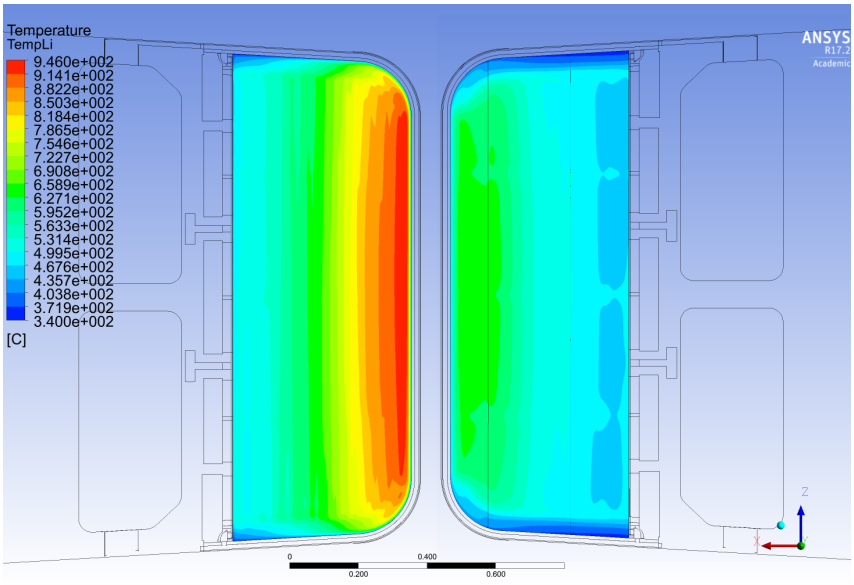

Figure 27: Temperature distribution of the pebble beds on the lithium orthosilicate (left) and beryllium (right) side with $\dot{m}_{CO_2} = 0.23 \frac{kg}{s}$

However, looking at the temperature distribution of the CO_2 shows potential problems of the chosen mass flow. While the maximum temperature of the CO_2 in the cooling channels

both in the first wall and the cooling plate are low enough to allow for a sufficient cooling of the material, the outlet temperature of the cooling loop is only 480.1°C, already below the aspired exit temperature of 500°C. A further increase of the overall mass flow would further lower this temperature, making power generation more inefficient.

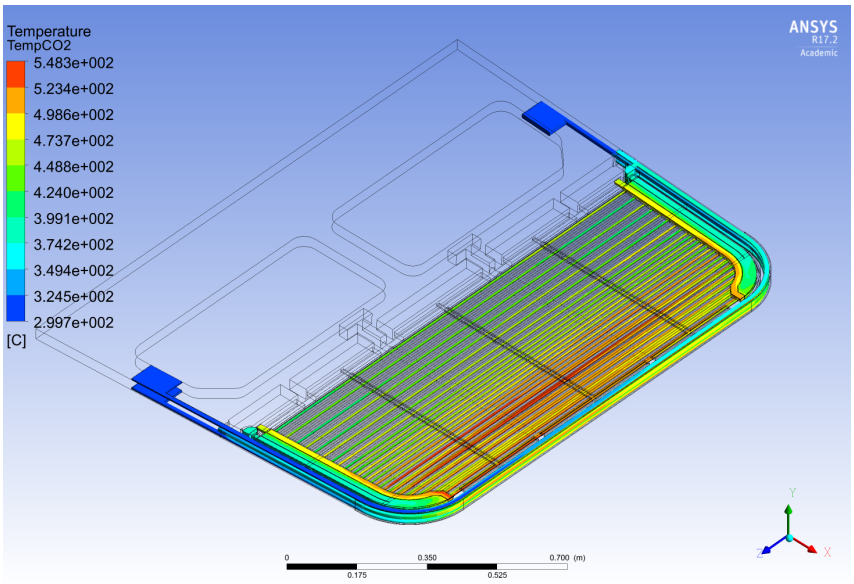

Figure 28: Temperature distribution of the CO_2 with $\dot{m}_{CO_2} = 0.23\frac{kg}{s}$

4.3 Simulation with Enhanced Heat Transfer

4.3.1 Enhancing the Heat Transfer in Cooling Channels

While there is a wealth of information and experiments done on enhanced heat transfer for helium cooling of the first wall, the same cannot be said for the topic of CO_2 cooling. As such, papers examining the influence of ribs and fins on air and helium flows were also taken into account for this section. A focus was put on papers looking at flows at high Reynolds numbers, because the Reynolds number in the first wall cooling channel is around 530000.

For angled transverse ribs, Raballandi et.al. [19] found that the increase in heat transfer fell with a rising Reynolds number. However, they still achieved a significant increase in the Nusselt number even with a Reynolds number of 400000. Ribs with a height of ¡10% of the hydraulic diameter of the channel showed the best thermal performance at high Reynolds numbers, especially when spaced more than 7.5 times rib height apart. Overall thermal performance *TP* suffered at Reynolds numbers greater than 100000 because the pressure loss penalty incurred by the roughness is greater than the increase in heat transfer.

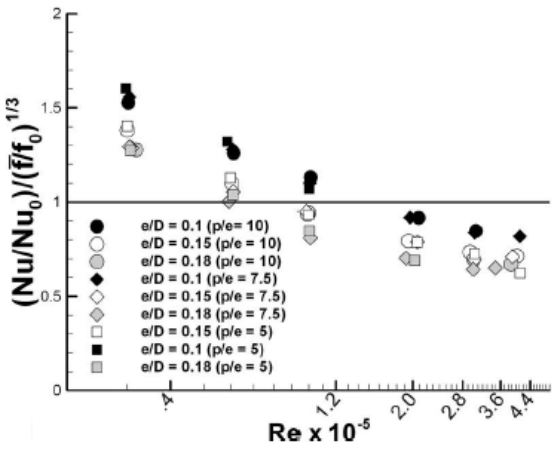

Figure 29: Thermal performance of 45° angled transverse ribs [19]

According to a study done by Alkhamis et.al. [20], V-shaped ribs offer better thermal performance than transverse ribs. The increase in Nusselt number is shown in Figure 30, while Figure 31 shows the overall thermal performance. It can easily be seen that the break-even point for V-shaped ribs is at Reynolds numbers around 200000, significantly higher than angled transverse ribs.

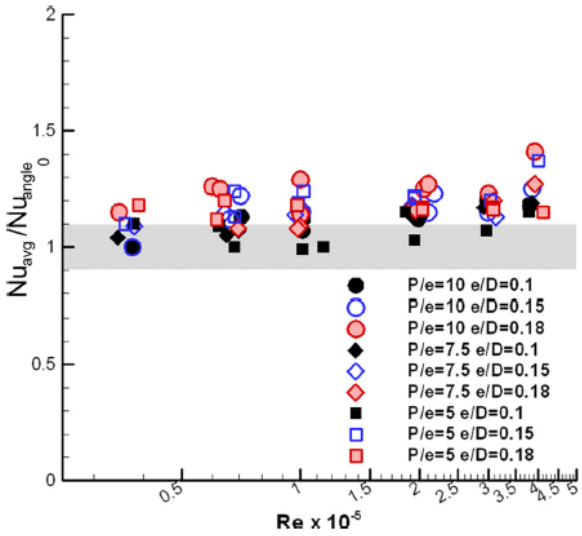

Figure 30: Comparison between Nusselt numbers with v-shaped and angled ribs [20]

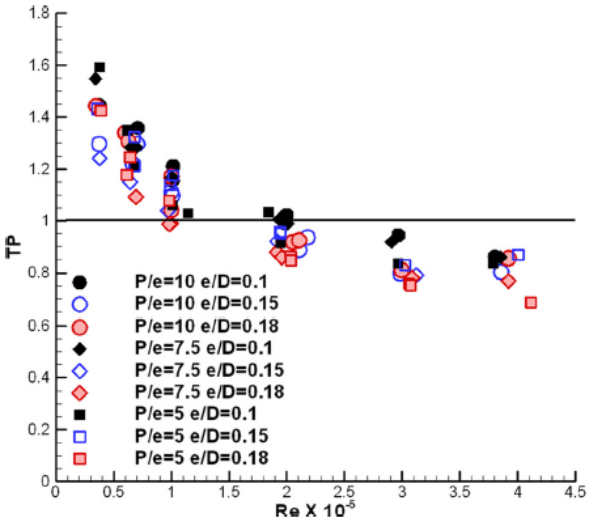

Figure 31: Thermal performance of 45° V-shaped ribs [20]

Interestingly, Han et.al. [21] found broken V-shaped ribs to have an even better thermal performance than normal V-shaped ribs. However, these experiments were only done up to a Reynolds number of 90000, so further investigation is necessary to determine if this behaviour is also present at the significantly higher Reynolds numbers present in the first wall cooling channel.

It should also be noted that $\bar{f}$ remains constant independent of the Reynolds number. However, $\frac{\bar{f}}{f_0}$ increases with increasing Reynolds numbers, since f_0 falls with increasing Reynolds number. Assuming a rib height of $0.1D_h$, $\bar{f}$ is given by

$$\bar{f} = 1.76 \left(\frac{P}{e}\right)^{-0.51} \left(\frac{e}{D_h}\right)^{1.14} \tag{69}$$

where P is the distance between the ribs.

4.3.2 Simulation with Increased Wall Roughness

Simulating the BB slice with ribs on the channel walls would take considerably more processing power and time, since the secondary flows induced by those ribs need to be resolved accurately to gain reliable information about the heat transfer in the BB. Due to these difficulties, a simulation was done where the sand grain roughness of the channel walls was increased to simulate the increased friction factor caused by ribs. This allows an approximation of the increase in circulating power by looking at the increased pressure drop over the BB slice.

It is also expected that the heat transfer will already be enhanced by increasing the roughness of the wall. However, this effect will most likely not be large enough to keep the BB within its temperature design limits. This is not necessarily a problem, since

artificial roughnesses like ribs usually provide a higher increase in heat transfer than an unstructured roughness that is equivalent in friction factor.
A rib height of $e = 0.1D_h$ and a rib spacing of $\frac{P}{e} = 7.5$ was chosen due to the results achieved by Alkhamis et.al. [20]. Using correlation from their paper this gives us a friction factor of $\bar{f} = 0.0456$. The Reynolds number in the first wall cooling channel is $Re_{FW} = 531500$, in the cooling plate channels it is $Re_{CP} = 91500$. Using the Moody chart, this gives us an equivalent sand grain roughness for the first wall channel of 187.5 micron. However, since in the experiments done by Alkhamis two walls of the channel were covered with ribs whereas only the front wall of the channel will be covered in the BB, the roughness value used in the simulation is 93.75 micron. For the cooling plate channels, the equivalent sand grain roughness is 56.25 micron.

The results of the simulation show a significant decrease in the temperature of the first wall. It stays under its design limit of 550°C, reaching a maximum temperature of 549.0°C. However, the temperatures in the cooling plate are virtually unchanged compared to the original simulation without increased wall roughness. The maximum temperature in the cooling plate is 589.5°C. The hotspot is still in the front third of the BB.

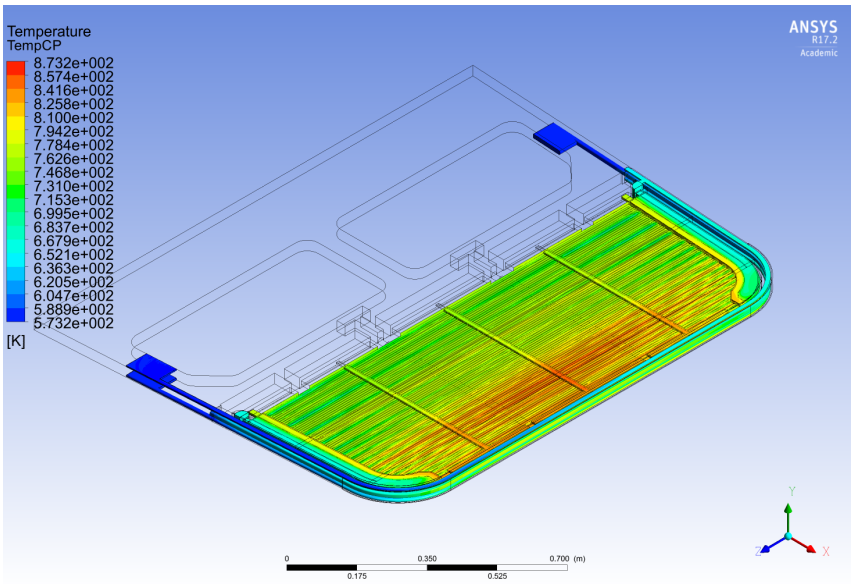

Figure 32: Termperature distribution in the cooling plate and first wall with increased wall roughness

Since the temperature in the cooling plate has changed only marginally, it is unsurprising that the temperatures in the lithium orthosilicate and beryllium pebble beds are also very close to the original simulation. The maximum temperature reached in the lithium orthosilicate is 963.8°C while the beryllium reaches 683.9°C.

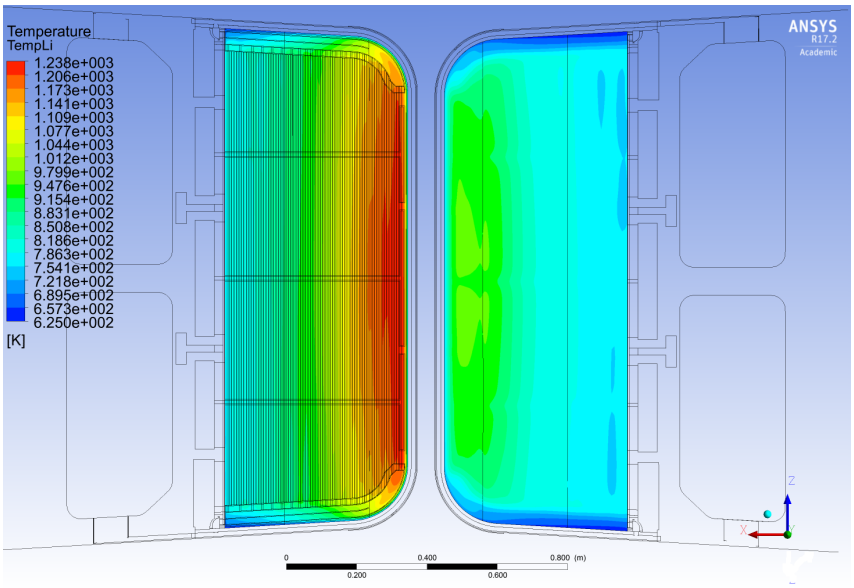

Figure 33: Temperature distribution of the pebble beds on the lithium orthosilicate (left) and beryllium (right) side with increased wall roughness

The bulk CO_2 temperature in the first wall remains unchanged while the peak temperature reached close to the wall is significantly reduced to 494.0°C, which indicates a better mixing of the fluid due to increased turbulence. The same cannot be said for the cooling plate, where the CO_2 still reaches a maximum temperature of 580.6°C.

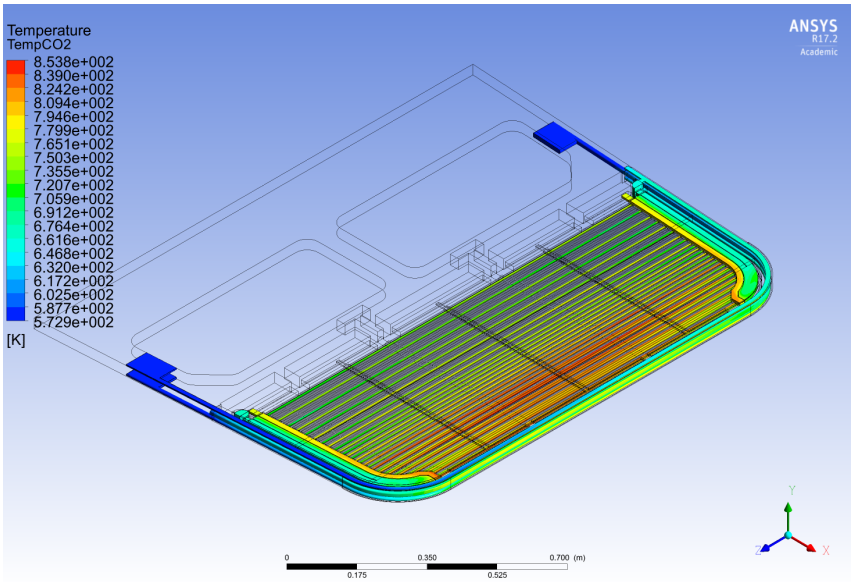

Figure 34: Temperature distribution of the CO_2 with increased wall roughness

The CO_2 in the cooling plate still fails to extract enough heat from the material to keep it sufficiently cold. This can be explained in part by the channel layout in the cooling plate. Since the channels are quite close together and use a counterflow setup as illustrated in Figure 35, the cold CO_2 entering the cooling plate in one half-loop is heated by the hot

CO_2 leaving the cooling plate in the other half-loop. This means that an increase in heat transfer between solid and liquid by introducing an artificial roughness into the channels will not be able to solve the problem that is the overheating of the blanket materials. The counterflow channels act as a heat exchanger, leading to the peak in temperatures in the middle of the blanket.

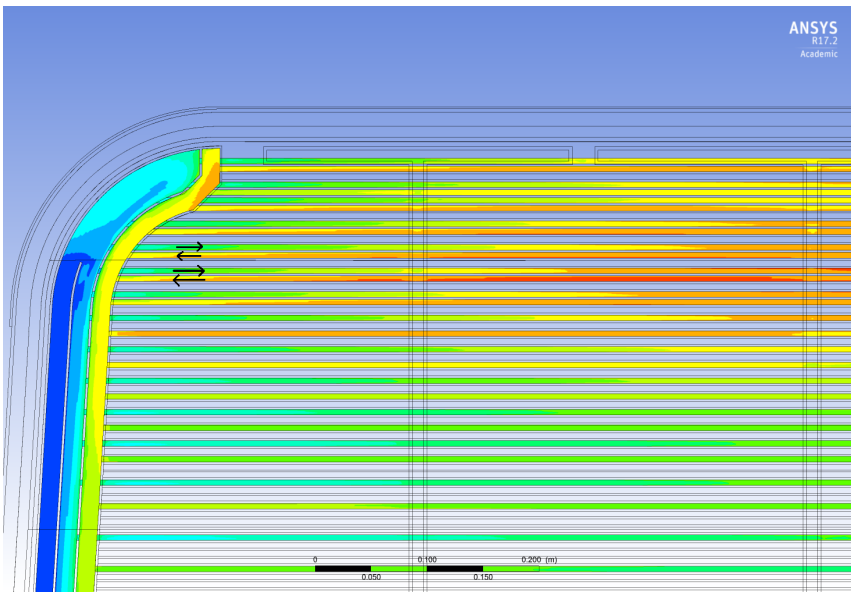

Figure 35: Counterflow scheme in the cooling plate

Increasing the overall mass flow of CO_2 is discouraged because it negatively impacts the outlet temperature of the coolant, leading to a less efficient power generation. Notably, the first wall can be cooled with a mass flow of $\dot{m}_{CO_2} = 0.1992\frac{kg}{s}$ and an increased channel wall roughness. This means that the counterflowing cooling plate channels need to be thermally isolated from each other to avoid the peak in coolant temperature in the middle of the blanket. A potential solution for this problem is the redesign of the channel layout in the cooling plate, separating the counterflowing channels with a blind channel to inhibit heat transfer between them, as shown in Figure 36. Another possibility is changing the direction of the cooling plate cooling channels, having them run perpendicular to their current orientation. By having the cooling fluid flow from the front of the BB to the back, the coolant would first encounter the hottest part of the BB, allowing it it cool the most critical spots better.

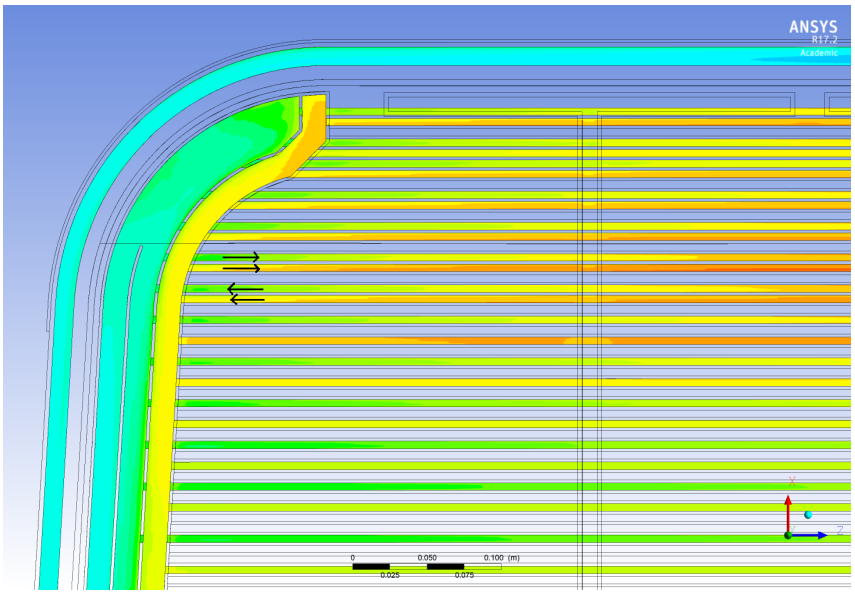

Figure 36: Counterflow scheme with thermally isolated cooling channels

4.4 Circulating Power Calculation

First the circulating power necessary for helium cooling of the blanket is calculated for comparison purposes. The total pressure drop over the blanket when cooled with a helium mass flow of $\dot{m}_{He} = 0.046\frac{kg}{s}$ is $\Delta p_{He} = 0.17MPa$. With the density of the helium in the first wall being on average $\rho_{He} = 6.39\frac{kg}{m^3}$, the pumping power necessary to pump the helium through the BB slice is

$$P_{He} = \frac{\dot{m}_{He}\Delta p_{He}}{\rho_{He}} = 1.22kW \tag{70}$$

Doing the same for a CO_2 mass flow of $\dot{m}_{CO_2} = 0.1992\frac{kg}{s}$ yields a circulating power of

$$P_{CO_2} = 0.734kW \tag{71}$$

with $\rho_{CO_2} = 72.21\frac{kg}{m^3}$ and $\Delta p_{CO_2} = 0.266MPa$.

One should also take into account the additional pressure loss caused by the artificial roughness in the first wall cooling channel. Taking a rib spacing value of $\frac{P}{e} = 7.5$ and using the correlation found by Alkhamis et.al. (see Equation (69)), we obtain a friction factor of

$$\bar{f}_{FW} = 0.0456 \tag{72}$$

The original simulation was done by setting the sand grain roughness of the channel walls

to 13.49μm. With a Reynolds number of 530000 in the first wall cooling channel, the Moody chart gives us a friction factor of

$$f_{0,FW} = 0.02 \tag{73}$$

Since the pressure drop is linearly correlated to the friction factor, we can calculate the additional pressure drop caused by the artificial roughness by using the difference between the two friction factors.

$$\Delta P_{AR,FW} = (\bar{f}_{FW} - f_{0,FW})\frac{\rho_{CO_2} u_{FW}^2}{2}\frac{L}{D_h} = 0.0256\frac{\rho_{CO_2}\left(\frac{\dot{m}_{FW,CO_2}}{\rho_{CO_2} A_{FW}}\right)^2}{2}\frac{L}{D_h} = \tag{74}$$
$$= 0.0256\frac{\dot{m}_{FW,CO_2}^2}{\rho_{CO_2} A_{FW}^2}\frac{L}{D_h} = 0.026MPa$$

This assumes that a lenght of 1m of the first wall cooling channel has ribs added to it. With this additional pressure drop, the total circulating power necessary for CO_2 cooling with ribs in the first wall cooling channel is

$$P_{CO_2}^* = P_{CO_2} + P_{AR,FW} = 0.805kW \tag{75}$$

Finally, the channels in the cooling plate are artificially roughened as well. Repeating the same process for these channels as for the first wall cooling channel gives us the following values:

$$\bar{f}_{CP} = 0.0456 \tag{76}$$
$$Re_{CP} = 91500 \tag{77}$$
$$f_{0,CP} = 0.028 \tag{78}$$

$$\Delta P_{AR,CP} = (\bar{f}_{CP} - f_{0,CP})\frac{\rho_{CO_2} u_{CP}^2}{2}\frac{L}{D_h} = 0.0176\frac{\rho_{CO_2}\left(\frac{\dot{m}_{CP,CO_2}}{\rho_{CO_2} A_{CP}}\right)^2}{2}\frac{L}{D_h} = \tag{79}$$
$$= 0.0176\frac{\dot{m}_{CP,CO_2}^2}{2\rho_{CO_2} A_{CP}^2}\frac{L}{D_h} = 0.704MPa$$

This assumes a lenght of 15m of roughened wall distributed in the cooling channels.

So the total circulating power taking into account the increased roughness in both the first wall and the cooling channels is

$$P_{CO_2,total} = P_{CO_2}^* + P_{AR,CP} = 0.934kW \tag{80}$$

This number agrees very well with the number the simulation gives. In the simulation with increased wall roughness, the pressure loss over the blanket is 0.336MPa. With a mass flow of $\dot{m}_{CO_2} = 0.1992\frac{kg}{s}$ and a density of $\rho_{CO_2} = 72.21\frac{kg}{m^3}$, we get

$$P_{CO_2,total,sim} = 0.926kW \tag{81}$$

5 Conclusion

Based on the simulations done in this thesis and the available data on the effect of artificial roughnesses in cooling channels, CO_2 cooling does seem to offer a significant advantage over helium cooling as far as circulating power is concerned. However, it also necessitates the use of artificial roughnesses to sufficiently cool the blanket, increasing the manufacturing costs. Additionally, a redesign of the channel distribution in the less thermally loaded parts of the cooling plate seems necessary to achieve a sufficiently high heat transfer in the cooling plate cooling channels.

If the possibility of CO_2 cooling for a pebble bed breeding blanket of a nuclear reactor should be explored further in the future, more experiments need to be done on the heat transfer behaviour of CO_2 at high Reynolds numbers with artificial roughnesses. A redesign of the cooling channel distribution offers the chance of achieving satisfying cooling results with a mass flow of CO_2 that offers a significant advantage with regards to circulating power.

6 References

[1] R. Nave, Georgia State U.: *Calculation of Coulomb Barrier.* – http://hyperphysics.phy-astr.gsu.edu/hbase/NucEne/coubar.html

[2] Darling, D.: *binding energy.* – http://www.daviddarling.info/encyclopedia/B/binding_energy.html

[3] Richard Bonomo, University of W.: *Inertial Electrostatic Confinement Fusion.* – http://iec.neep.wisc.edu/operation.php

[4] Moynihan, Dr. Matthew J.: *Basic Magnetic Mirror.* – https://en.wikipedia.org/wiki/File:Basic_Magnetic_Mirror.jpg

[5] Plasmaphysik, Max-Planck I.: *W7X-Spulen Plasma blau gelb.* – https://en.wikipedia.org/wiki/File:W7X-Spulen_Plasma_blau_gelb.jpg

[6] alternatives, Commissariat : *Magnetic configuration of the tokamak.* – http://www-fusion-magnetique.cea.fr/gb/fusion/physique/configtokamak.htm

[7] Fischer, Dr. U.: *Neutronenphysik.* – Lecture slides

[8] Joel H. Ferziger, Milovan P.: *Computational methods for fluid dynamics.* Berlin : Springer, 2002

[9] Gabriel Staffelbach, Gicquel L.Y.M. Thierry P. Jean Mathieu Senoner S. Jean Mathieu Senoner: *Large Eddy Simulation of Combustion on Massively Parallel Machines.* 2008

[10] Moin, Parviz ; Mahesh, Krishnan: Direct Numerical Simulation: A Tool in Turbulence Research. In: *Annual Review of Fluid Mechanics* (1998). – http://www.annualreviews.org/doi/abs/10.1146/annurev.fluid.30.1.539

[11] Díez, Nerea: *CFD-Untersuchungen der Kühlung eines Solar-Absorberrohres mit ungleichmäßiger Wärmeflussverteilung in Umfangsrichtung*, KIT, Diplomarbeit, 2012

[12] Schwarze, Rüdiger: *CFD-Modellierung: Grundlagen und Anwendungen bei Strömungsprozessen.* Berlin : Springer, 2013

[13] Chaitanya, Krishna: *Boundary Layer Modeling using Inflation Layers.* – http://www.cadfem.in/blog/organic/fbu/modeling-boundary-layer-inflation/

[14] Robert Stieglitz, Volker H.: *Thermische Solarenergie: Grundlagen, Technologie, Anwendungen.* Berlin : Springer, 2012

[15] Online, CFD: *Law of the wall*. 2011. – https://www.cfd-online.com/Wiki/Law_of_the_wall

[16] Xiande Fang, Zhanru Z. Yu Xu X. Yu Xu: New correlations of single-phase friction factor for turbulent pipe flow and evaluation of existing single-phase friction factor correlations. In: *Nuclear Engineering and Design* (2011). – http://www.sciencedirect.com/science/article/pii/S0029549311000173

[17] Luai Al-Hadhrami, Je-Chin H. Todd Griffith G. Todd Griffith: Heat Transfer in Two-Pass Rotating Rectangular Channels (AR=2) With Five Different Orientations of 45 Deg V-Shaped Rib Turbulators. In: *Journal of Heat Transfer* (2003). – http://heattransfer.asmedigitalcollection.asme.org/article.aspx?articleid=1446334

[18] standards, National I. ; Technology: *NIST Chemistry WebBook*. – http://webbook.nist.gov/chemistry/

[19] Akilesh P. Raballandi, Je-Chin H. Huitao Yang Y. Huitao Yang: Heat Transfer and Pressure Drop Correlations for Square Channels With 45 Deg Ribs at High Reynolds Numbers. In: *Journal of Heat Transfer* (2009). – http://heattransfer.asmedigitalcollection.asme.org/article.aspx?articleid=1475126

[20] Nawaf Y. Alkhamis, Je-Chin H. Akilesh P. Raballandi R. Akilesh P. Raballandi: Heat Transfer and Pressure Drop Correlations for Square Channels With V-Shaped Ribs at High Reynolds Numbers. In: *Journal of Heat Transfer* (2011). – http://heattransfer.asmedigitalcollection.asme.org/article.aspx?articleid=1450314

[21] J.C. Han, Y.M Z.: High performance heat transfer ducts with parallel broken and V-shaped broken ribs. In: *International Journal of Heat and Mass Transfer* (1992). – http://www.sciencedirect.com/science/article/pii/0017931092902862

Erklärung

Hiermit versichere ich, dass ich meine Abschlussarbeit selbständig verfasst und keine anderen als die angegebenen Quellen und Hilfsmittel benutzt habe.

Datum: 31.08.2017 .....

(Unterschrift)